The Dendrites of CA2 and CA1 Pyramidal Neurons Differentially Regulate Information Flow in the Cortico-Hippocampal Circuit

Kalyan V. Srinivas,[1] Eric W. Buss,[1,4] Qian Sun,[1] Bina Santoro,[1] Hiroto Takahashi,[1] Daniel A. Nicholson,[4] and Steven A. Siegelbaum[1,2,3]

[1]Department of Neuroscience, [2]Department of Pharmacology, and [3]Kavli Institute for Brain Science, Columbia University, New York, New York 10032, and [4]Department of Neuroscience, Rush University Medical Center, Chicago, Illinois 60612

The impact of a given neuronal pathway depends on the number of synapses it makes with its postsynaptic target, the strength of each individual synapse, and the integrative properties of the postsynaptic dendrites. Here we explore the cellular and synaptic mechanisms responsible for the differential excitatory drive from the entorhinal cortical pathway onto mouse CA2 compared with CA1 pyramidal neurons (PNs). Although both types of neurons receive direct input from entorhinal cortex onto their distal dendrites, these inputs produce a 5- to 6-fold larger EPSP at the soma of CA2 compared with CA1 PNs, which is sufficient to drive action potential output from CA2 but not CA1. Experimental and computational approaches reveal that dendritic propagation is more efficient in CA2 than CA1 as a result of differences in dendritic morphology and dendritic expression of the hyperpolarization-activated cation current (I_h). Furthermore, there are three times as many cortical inputs onto CA2 compared with CA1 PN distal dendrites. Using a computational model, we demonstrate that the differences in dendritic properties of CA2 compared with CA1 PNs are necessary to enable the CA2 PNs to generate their characteristically large EPSPs in response to their cortical inputs; in contrast, CA1 dendritic properties limit the size of the EPSPs they generate, even to a similar number of cortical inputs. Thus, the matching of dendritic integrative properties with the density of innervation is crucial for the differential processing of information from the direct cortical inputs by CA2 compared with CA1 PNs.

Key words: CA2 pyramidal neuron; dendrites; glutamate uncaging; passive properties; two-photon imaging

---

Significance Statement

Recent discoveries have shown that the long-neglected hippocampal CA2 region has distinct synaptic properties and plays a prominent role in social memory and schizophrenia. This study addresses the puzzling finding that the direct entorhinal cortical inputs to hippocampus, which target the very distal pyramidal neuron dendrites, provide an unusually strong excitatory drive at the soma of CA2 pyramidal neurons, with EPSPs that are 5–6 times larger than those in CA1 pyramidal neurons. We here elucidate synaptic and dendritic mechanisms that account quantitatively for the marked difference in EPSP size. Our findings further demonstrate the general importance of fine-tuning the integrative properties of neuronal dendrites to their density of synaptic innervation.

Introduction

Cortical pyramidal neurons (PNs) receive thousands of excitatory inputs from different brain regions that often target distinct den-

dritic compartments (Magee, 2000; Gulledge et al., 2005; Spruston, 2008). Inputs from nearby regions tend to target proximal dendrites close to the soma, whereas inputs from distant regions target distal dendrites (Magee, 2000; London and Häusser, 2005; Spruston, 2008; Stuart and Spruston, 2015). This pattern is apparent in hippocampus, where excitatory inputs from local hippocampal regions form synapses on PN proximal dendrites in stratum radiatum (SR) and stratum oriens (SO), whereas direct inputs from entorhinal cortex

(EC) target PN distal dendrites in stratum lacunosum moleculare (SLM) (Witter et al., 2014).

Much is now known about the function and behavioral roles of the PNs in the hippocampal CA3 and CA1 subregions (Witter et al., 2014). However, far less is known about the properties of the PNs in the hippocampal CA2 subregion, which was recently found to play a critical role in social memory storage (Hitti and Siegelbaum, 2014; Stevenson and Caldwell, 2014; Smith et al., 2016), aggression (Pagani et al., 2015), spatial encoding (Mankin et al., 2015; Kay et al., 2016) and novelty detection (Alexander et al., 2016).

Although the PNs of all three CA fields share a common dendritic distribution of distal cortical and proximal hippocampal inputs, the efficacy of these inputs is strikingly different. Thus, in both CA1 and CA3, the direct EC inputs provide only weak excitatory drive at the PN soma, in contrast to the much stronger excitation from the intrahippocampal input (Yeckel and Berger, 1995; Chevaleyre and Siegelbaum, 2010). As a result, the EC inputs primarily act to modulate excitation of CA1 PNs by their Schaffer collateral (SC) inputs from CA3 PNs (Magee, 2000; Spruston, 2008), promoting burst firing (Bittner et al., 2015) and the induction of heterosynaptic plasticity that enhances SC excitation (Dudman et al., 2007; Basu et al., 2013) and improves the specificity of contextual memory (Basu et al., 2016).

In contrast, the direct EC inputs to CA2 generate surprisingly powerful EPSPs at the CA2 PN soma that are 5- to 6-fold larger than EPSPs in CA1 PNs (Chevaleyre and Siegelbaum, 2010). With strong EC stimulation, the CA2 distal EPSP is further amplified by the firing of dendritic Na^+ spikes, which propagate efficiently to the CA2 PN soma to trigger action potential output (Sun et al., 2014). Although distal dendritic spikes can also be triggered in CA1 PNs (Gasparini et al., 2004; Golding et al., 2005), these spikes are greatly attenuated by CA1 dendrites and normally fail to trigger a spike output (Sun et al., 2014). Sun et al. (2014) determined that differences in the architecture of dendritic branching play an important role in enhancing dendritic spike amplitude at the CA2 compared with CA1 soma.

Here we focus on the mechanisms responsible for the 5- to 6-fold difference in the subthreshold somatic EPSP evoked by cortical inputs in CA1 versus CA2 PNs. We explored this question using a multidisciplinary approach of whole-cell somatic and dendritic patch-clamp recordings, two-photon glutamate uncaging at single spines, serial section postembedding immunogold electron microscopy, and morphologically realistic multicompartment neuronal simulations. Our results reveal that the larger cortical EPSP in CA2 compared with CA1 PNs results from three factors: (1) a decreased level in CA2 of dendritic expression of the hyperpolarization-activated cation current, I_h, (2) an increased number of EC inputs to the CA2 distal dendrites, and (3) differences in dendritic morphology. We further show that the appropriate matching of dendritic integrative properties to the number of synaptic inputs is critically important in enabling the CA2 PNs to respond to their larger number of distal inputs. In this manner, CA2 PNs are able to participate in an efficient disynaptic circuit in which strong excitation by the EC inputs triggers CA2 output to excite its downstream CA1 target.

Materials and Methods

Hippocampal slice preparation. Transverse hippocampal slices were prepared from 5- to 6-week-old C57BL6 male mice. All experiments were performed on slices taken from dorsal hippocampus. We obtained 5 slices starting at the extreme dorsal end, and performed recordings on all but the most dorsal slice. In brief, mice were deeply anesthetized with

isoflurane and killed by decapitation in accordance with institutional regulations. Hippocampi were removed by dissection and transverse slices (400 μm thick) were cut on a vibratome (Leica VT1200S or Leica VT1000) in ice-cold dissection solution containing the following (in mM): 10 NaCl, 1.25 NaH$_2$PO$_4$, 2.5 KCl, 26 NaHCO$_3$, 10 glucose, 0.5 CaCl$_2$, 7 MgCl$_2$, 190 sucrose, and 2 Na-pyruvate. The slices were then transferred to 30°C ACSF (in mM) as follows: 125 NaCl, 2.5 KCl, 10 glucose, 26 NaHCO$_3$, 1.25 NaH$_2$PO$_4$, 2 Na-pyruvate, 2 CaCl$_2$, and 1 MgCl$_2$ for 30 min and then kept at room temperature for at least 1.5 h before transfer to the recording chamber. Dissection and ACSF were both saturated with 95% O$_2$ and 5% CO$_2$, pH 7.4.

Electrophysiology and recordings solutions. The recording ACSF had the following composition (mM): 125 NaCl, 1.25 NaH$_2$PO$_4$, 2.5 KCl, 26 NaHCO$_3$, 10 glucose, 2 CaCl$_2$, and 1 MgCl$_2$. Patch-clamp whole-cell recordings were obtained in current-clamp mode from CA1 and CA2 PNs in submerged slices at 33°C-35°C. Neurons were held at −70 mV with a patch pipette (3–5 MΩ) containing the following (in mM): 135 KMeS0$_4$, 5 KCl, 0.1 EGTA-Na, 10 HEPES, 2 NaCl, 5 ATP, 0.4 GTP, 10 phosphocreatine, pH 7.2 (290–300 mOsm). For imaging experiments, AlexaFluor-594 (25 μM) dye was included in the intracellular solution. Series resistance (typically 15–25 MΩ) was monitored throughout each experiment. Neurons with more than a 15% change in series resistance were excluded from analysis. Capacitance was fully compensated throughout the experiment. Fluorescent indicators (Alexa-594 cadaverine) were purchased from Invitrogen, diluted into 100× stock solution using standard intracellular solution, aliquoted, and frozen (20°C). In all experiments, inhibitory transmission was blocked by the GABA$_A$ and GABA$_B$ receptor antagonists SR 95531 (2 μM) and CGP 55845 (1 μM), respectively. Pharmacological antagonists were added to the bath solution by dilution from stock solutions. All drugs were obtained from either Sigma or Tocris Bioscience.

Electrophysiological data acquisition and analysis. Recordings were obtained using a two-channel Multiclamp 700B amplifier (Molecular Devices). Data were digitized on a Windows PC using an ITC-18 A/D board (Instrutech Instruments) controlled by either pClamp 9 software (Axon) or Axograph (Wavemetrics). All current-clamp data were acquired at 20 kHz and low-pass filtered at 4 kHz using the Multiclamp 700B Bessel filter. Analysis was performed using custom routines written in Igor Pro and MATLAB. Statistical tests were performed using Excel (Microsoft) and Prism (GraphPad). Statistical comparisons were performed using Student's t test. Results are expressed as mean ± SEM.

CA2 and CA1 PN reconstructions. Neurons were filled with biocytin (1%) using a patch pipette, and the biocytin was allowed to diffuse for >15 min. The slices were fixed and kept overnight in 4% PFA in 0.1 M phosphate buffer at 4°C. The slices were then rinsed five times for 5 min in 0.1 M phosphate buffer, kept in 1% hydrogen peroxide in 0.1 M phosphate buffer for 30 min, and then rinsed three times in 0.02 M potassium phosphate saline (KPBS) for 30 min. Slices were kept overnight on the shaker in avidin-biotin-peroxidase complex solution and rinsed three times in 0.02 M KPBS for 30 min. Each slice was then placed in DAB (0.7 mg/ml 3,3″-diaminobenzidine, hydrogen peroxide, 0.06 M Tris buffer in 0.02 M KPBS) until the slice turned light brown and then transferred to 0.02 M KPBS. Slices were transferred again to fresh 0.02 M KPBS. Finally, the stained slices were rinsed in 0.02 M KPBS for 30 min on a shaker. Each slice was observed under a light microscope and then mounted onto a slide using crystal mount (Fino and Yuste, 2011).

Neurons with robust staining of the dendritic tree were reconstructed using Neurolucida software (MicroBrightField). The neurons were viewed with a 63× oil objective on a Zeiss upright light microscope. The neuron's processes were traced manually while the program recorded the coordinates of the tracing to create a digital 3D reconstruction. Whole-cell reconstructions included the soma and dendritic shafts, but not dendritic spines.

Spine densities were calculated as the number of spines divided by the length of the segment using a 100× objective. Dendritic segments having a dark stain with clearly visible spines, including no branch points and planar along the horizontal axis were chosen for spine density calculations. Because spine density varies with location (Megías et al., 2001), we determined spine densities from different regions of dendritic branch

segments of the CA2 and CA1 PNs, namely, SLM thin and medium diameter branches, SR thin branches, SR thick distal and proximal branches, and SO. To account for spines obscured from view by the dendritic shaft, spine densities were corrected using the geometric equation derived in Feldman and Peters (1979) as follows:

$$\cos\theta = \frac{Dr + Sd}{Dr + Sl}$$

$$N = \frac{n\pi[(Dr + Sl)^2 - (Dr + Sd)^2]}{[\theta\pi/90 * (Dr + Sl)^2] - 2[(Dr + Sl)\sin\theta(Dr + Sd)]}$$

where N is the estimated spine density, n is the raw spine density, before accounting for hidden spines, Dr is the radius of dendrite, Sl is the average length of spines (0.7 μm), and Sd is the average diameter of spine head (0.35 μm).

Immunohistochemistry. Animals were perfused with ice-cold 1× PBS followed by 4% PFA in 1× PBS; 40 μm coronal slices were cut with a vibratome, and permeabilized in PBS + 0.1% Triton, followed by incubation in blocking solution (1× PBS + 3% normal goat serum). Primary antibody incubation was performed in blocking solution overnight at 4°C. Antibodies used were as follows: rat monoclonal anti-HCN1 (clone RQT 7C3, EMD Millipore); mouse monoclonal anti-HCN2 (clone N71/37, NeuroMab); and rabbit polyclonal anti-PCP4 (HPA005792, Sigma). Secondary antibodies were as follows: goat anti-rat Alexa-647 preadsorbed (ab150167, Abcam); goat anti-mouse IgG1 Alexa-488 (Invitrogen); and goat anti-rabbit Alexa-488 and goat anti-rabbit Alexa-546 (Invitrogen). Fluorescence imaging was performed on a laser scanning confocal microscope (Zeiss LSM 700). All images were analyzed using ImageJ software and data plotted in Microsoft Excel.

TRIP8b knock-out mouse. TRIP8b knock-out mice were generated through the National Institutes of Health KOMP mutagenesis project. Details of the targeting strategy can be found at www.komp.org (project ID CSD83859; allele Pex5l$^{tm1a(EUCOMM)Wtsi}$: CSD knock-out first, promoter driven, with loxP sites flanking exon 8 of the Pex5l mouse gene). In the MGI database, the mouse gene encoding TRIP8b is named Pex5l. Homologous recombination was performed in ES cell line KV1 (129B6 hybrid). Heterozygous Pex5l$^{tm1a(EUCOMM)Wtsi}$ mice were crossed to germline Flp-expressing mice (Tg(ACTFLPe)9205Dym/J, The Jackson Laboratory stock #005703), resulting in deletion of the frt-flanked lacZ-neo cassette in the offspring mice, and thus in a conditional Pex5l$^{flox/+}$ allele. Heterozygous Pex5l$^{flox/+}$ mice were then crossed to germline Cre-expressing mice (Tg(CMV-cre)1Cgn/J, The Jackson Laboratory stock #06054) to obtain a TRIP8b knock-out allele (Pex5l$^{+/-}$). Deletion of exon 8 leads to a frameshift mutation in the coding sequence with the formation of an unstable TRIP8b protein. A similar strategy was used to obtain a previously published TRIP8b knock-out line (Lewis et al., 2011), which carries a deletion of exon 6 and exon 7, resulting in a frameshift mutation and an unstable TRIP8b protein. Pex5l$^{+/-}$ mice were backcrossed to wild-type C57BL/6J mice for 3 generations (N3), before heterozygote breedings were set up to obtain the TRIP8b$^{-/-}$ (knock-out) and TRIP8b$^{+/+}$ (wild-type) littermates used in the present study. To produce the data represented in Figure 3B, three wild-type/homozygous TRIP8b-knock-out littermate animal pairs were used ($n = 3$ per genotype). Only wild-type animals were used for Figure 3A ($n = 3$).

Computer model of reconstructed neurons. Three-dimensional whole CA1 and CA2 PN reconstructions, including measured dendritic diameters and lengths, were imported into the NEURON simulation environment (Hines and Carnevale, 1997). The CA1 and CA2 models incorporated identical standard values for passive membrane properties ($R_m = 40,000$ Ω-cm^2, $C_m = 1$ μF/cm^2, $R_i = 150$ Ω-cm) (Harnett et al., 2012).

To account for the extra surface area due to spines, in each dendritic segment R_m was divided by and C_m multiplied by a "spinescale" parameter (Stuart and Spruston, 1998; Golding et al., 2005; Routh et al., 2009). The spinescale parameters were calculated using corrected spine densities, dendritic diameters, and previously reported spine surface area measurements (Harris and Stevens, 1989). Spinescale was defined as the ratio

of the total surface area, including spines, to the surface area without spines, according to the following equation:

$$\text{SpineScale} = \frac{SA_{\text{Shaft}} + SA_{\text{Spine}}}{SA_{\text{Shaft}}} = \frac{\pi d + NA}{\pi d}$$

where SA_{shaft} is the surface area of dendritic shaft for a 1-μm-long segment, SA_{spines} is the surface area contributed by spines in a 1-μm-long segment, d is the average diameter of dendritic shaft, N is the estimated spine density from the Feldman and Peters (1979) equation, and A is the average surface area of an individual spine.

The average surface area of an individual spine was set to 0.85 μm^2, which is the sum of the head and neck surface areas reported for rats by Harris and Stevens (1989). Spinescale values for each dendritic region ranged from 1.0 (for regions with no spines) to 2.75 (in locations with thin dendrites and many spines). After applying the spinescale, the R_{input} value of the model closely matched our experimentally determined R_{input} values for both CA1 and CA2 PNs.

The only active conductance included in the model was the I_h conductance (G_h). The voltage-dependent kinetics incorporated in the model were similar to ones previously reported (Magee, 1998). The reversal potential was set to −25 mV (Magee, 1998). I_h dendritic distribution was consistent with the available experimental data on CA1 neurons (Magee, 1998; Poolos et al., 2002) and from our immunohistochemistry results from mouse CA1 PNs (see Fig. 3). For CA1 PNs, G_h was implemented as a linear density gradient increasing 7.0-fold as a function of distance from the soma, reaching a maximal value at distances >350 μm from the soma, as previously described (Magee, 1998). For CA2 PNs, we used a constant uniform value of G_h, consistent with our immunohistochemistry results (see Fig. 3). Furthermore, simulation results in which I_h was distributed uniformly or in a somatodendritic gradient support the view that I_h is uniformly expressed in CA2 dendrites (see Results). Conductance values were adjusted to match the measured voltage sag recorded in the CA2 and CA1 PN soma. Derived values of G_h at the soma were 0.000063 S/cm^2 for CA1 and 0.000012 S/cm^2 for CA2. The ratio for K$^+$ and Na$^+$ leak currents in each compartment was adjusted to attain a uniform resting membrane potential of −70 mV. For all I_h channels located in the dendritic compartments >100 μm away from the soma, was determined as follows:

$$I_h = g_h(V + 25)$$

$$g_h = \frac{g_{\text{max}}}{1 + \exp\left(\frac{V + 73}{8}\right)}$$

where V is in mV. The mid-point of activation (−73 mV) was shifted by 8 mV in the depolarizing direction from the value at soma, based on dendritic recordings made in hippocampal CA1 PNs (Magee, 1998).

Excitatory synapses. Excitatory synapses were distributed randomly on the distal dendritic arbor (>350 μm from the soma) of the reconstructed neuron. Each excitatory synaptic conductance was modeled using two exponential function (τ_{rise} of 0.1 ms and τ_{decay} of 1.5 ms), with a reversal potential of 0 mV, and a conductance of 0.0001 μS.

Modeling spines. In some simulations, an additional passive compartment consisting of a spine head (0.25 μm radius) with a neck (500 MΩ) was attached randomly onto distal branches in the neuron models. An excitatory synapse with a fixed conductance value (0.002 μS) was used to evoke an EPSP in spine head compartment in all simulations.

Modeling AMPA and NMDAR conductances at spines. The AMPA component was modeled as a conductance with a rising time constant of 0.5 ms and a single decay time constant of 3 ms. The NMDA component was modeled with a single exponential rising phase with a time constant of 7 ms and a double exponential decaying phase with time constants of 200 and 2000 ms, contributing 80% and 20% to the total decay amplitude, respectively. The voltage dependence of the NMDA receptor channels was modeled using below equations (Spruston et al., 1995). NMDA/AMPA ratio was adjusted to 2.5 for CA2 PNs and 5.75 for CA1 PNs at spine head to obtain 20% increase in somatic EPSP size as follows:

$$I = \frac{I_o}{1 + \frac{[\mathrm{Mg}^{2+}]_0}{K_o} \exp(-\delta z F V / RT)}$$

$$g = g_1 + (g_2 - g_1)/(1 + e^{-\alpha V})$$

where I_o is the current in Mg^{2+} free solution, K_o is the IC_{50} at 0 mV, α is the electrical distance of the Mg^{2+} binding site from the outside of the membrane, z is the valency of Mg^{2+}, F is the Faraday constant, R is the gas constant, T is absolute temperature, g is the conductance, g_1 is the lowest conductance (at very negative potentials) and g_2 is the highest conductance (at very positive potentials). Finally, $I_o = g(V - V_{\mathrm{rev}})$, where V is the membrane potential and V_{rev} is the reversal potential of the current.

Two-photon uncaging and imaging. Combined 2-photon uncaging of MNI-glutamate and 2-photon imaging was performed using a Prairie Technologies Ultima two-photon microscope. MNI-glutamate was included in the bath at 5 mM and glutamate uncaged using 500 μs pulses of 725 nm light (except where noted). AlexaFluor-594 was excited at 820 nm to visually identify spines. Spines on secondary and tertiary apical dendrites within 100 μm (proximal sites) and >350 μm (distal) of the soma were selected. In these experiments, test pulses were first delivered around the perimeter of the spine to determine the optimal site of uncaging. The power of the uncaging pulse was then set to bleach ~40% of the AlexaFluor-594 in the spine to achieve a uniform illumination intensity at the spine in different preparations (Bloodgood and Sabatini, 2007). With these laser settings, the uncaging EPSP (uEPSP) recorded at the soma was ~1 mV when glutamate was uncaged at proximal dendritic locations in SR. We used similar laser power to uncage glutamate at distal spines in SLM. Each spine was photostimulated 4 or 5 times (interstimulus interval >15 s) and the uEPSPs were averaged. Epifluorescent signals were collected through a 60× 1.1 NA objective (Olympus) and measured by GaAsP detectors (Hamamatsu). Optical signals were analyzed offline in ImageJ or Igor Pro (Wavemetrics).

Serial section postembedding immunogold electron microscopy. As described previously (Hitti and Siegelbaum, 2014), a Cre-dependent adeno-associated virus-expressing GFP was injected under stereotactic control into the CA2 region of adult *Amigo2-Cre* mice ($n = 3$), thereby limiting GFP expression to CA2 PNs. Two to 3 weeks later, mice were perfused transcardially with ice-cold 4% PFA/0.5% glutaraldehyde in 0.12 PBS. The hippocampus was then dissected, and hippocampal regions CA1 and CA2 were separately excised, cut into small rectangular slivers, and viewed with a fluorescence microscope. Slices for electron microscopy were obtained from dorsal hippocampus. GFP expression was confirmed visually in CA2 and confirmed to be absent in CA1. A micrograph was obtained of each sliver to aid with orientation following polymerization because the fluorescence emission of GFP is quenched during processing for freeze-substitution. The protein itself, however, is aldehyde-fixed, which allowed us to tag it with anti-GFP antibodies and immunogold particles. CA1 and CA2 slivers were then processed for freeze-substitution using a Leica EM CPC (Leica Microsystems) and AFS freeze-substitution system (Leica Microsystems), with Lowicryl HM20 (Electron Microscopy Sciences) as the polymer as described previously (Ganeshina et al., 2004; Neuman et al., 2015).

Following polymerization, slivers were trimmed for serial section electron microscopy. Using a Leica UC6 ultramicrotome, 25–45 serial sections were mounted on carbon/formvar-coated nickel slot grids (at 63 nm) and then prepared for postembedding immunogold labeling as described previously (Ganeshina et al., 2004; Neuman et al., 2015). Grids containing ribbons from CA2 or CA1 were immunostained in paired cohorts, using a mixture against the GluA family of glutamate receptors from Millipore, comprised of anti-GluA1 (AB1504; 3 μg/ml), antiGluA2 (AB1768; 1.5 μg/ml), anti-GluA2/3 (AB1506; 3 μg/ml), and anti-GluA4 (AB1508; 3 μg/ml) and a goat anti-GFP antibody (1:100; #600-101-215; Rockland). Following incubation and rinsing, grids were then incubated in a mixture of goat anti-rabbit (10 nm) and rabbit anti-goat (25 nm) immunogold particles (Ted Pella) diluted 1:50 in buffer. Systematic randomly located fields of SLM in CA2 and CA1 were then obtained using a JEOL 1200EX transmission electron microscope (JEOL) at 7×, 500×

magnification. Analyses are based on 143 CA1 axospinous synapses and 301 GFP-positive CA2 axospinous synapses, all of which were three-dimensionally reconstructed. To be considered GFP-positive, at least two 25 nm immunogold particles needed to be present within the spine head. Spine volumes and postsynaptic density (PSD) area measurements were performed as described previously (Nicholson and Geinisman, 2009).

Results

### Distal synaptic inputs provide stronger excitation of CA2 versus CA1 PNs

We evaluated the mechanisms by which synaptic drive from EC inputs produces a much larger somatic EPSP in CA2 compared with CA1 PNs by performing whole-cell somatic patch-clamp recordings in acute hippocampal slices (Chevaleyre and Siegelbaum, 2010; Sun et al., 2014). Neurons were filled with AlexaFluor-594 (25 μM) and imaged with two-photon laser-scanning microscopy for morphological identification (Fig. 1A). The identity of CA2 PNs was confirmed by their location along the transverse axis of the slice, which matches well with the identification based on molecular markers (Hitti and Siegelbaum, 2014), and distinct intrinsic electrophysiological properties (Chevaleyre and Siegelbaum, 2010; Sun et al., 2014). Thus, compared with CA1 PNs, CA2 PNs fired action potentials after a longer delay had a lower input resistance and a smaller depolarizing sag during a hyperpolarizing current step, which is caused by the activation of the hyperpolarization-activated cation current, I_h (Fig. 1B; Table 1).

Next, we confirmed previously reported differences in the magnitude of EPSPs recorded in CA2 and CA1 PNs in response to stimulation of their EC and SC inputs. As strong synaptic stimulation can elicit dendritic spikes and somatic action potentials, we restricted the stimulus strength to elicit subthreshold EPSPs. In addition, $GABA_A$ and $GABA_B$ receptors were blocked with SR 95531/CGP 55845 in all experiments to focus on EPSPs. As previously reported (Chevaleyre and Siegelbaum, 2010), stimulation of the EC inputs through an electrode placed in the distal apical dendritic region of SLM evoked EPSPs that were 5- to 6-fold larger in somatic recordings from CA2 compared with CA1 PNs (cells were current clamped to an initial holding potential of -70 mV). In contrast, stimulation of the SC inputs with an electrode in the proximal apical dendritic region of SR evoked a larger EPSP in CA1 compared with CA2 PNs (Fig. 1).

As the typical CA2 PN resting potential (-75 mV) is ~6 mV more negative than that of CA1 PNs (Table 1), we also evaluated the CA2 and CA1 EPSPs at the normal resting potentials. The EPSP measured at the normal CA2 PN resting potential (8.6 ± 0.5 mV) was ~10% larger than the CA2 EPSP measured at -70 mV (7.9 ± 0.45 mV; $n = 6$, $p < 0.01$, paired t test), consistent with the difference in EPSP driving force (Fig. 1E). In contrast, there was no statistically significant difference in EPSP size measured at the resting potential of CA1 PNs (-68.5 mV) compared that measured at -70 mV (1.36 ± 0.04 mV vs 1.39 ± 0.05 mV; $n = 6$, $p > 0.05$, paired t test) (Fig. 1F). Thus, differences in resting potential slightly enhance the difference in distally evoked EPSP amplitudes in CA2 compared with CA1 PNs.

Differential responses of CA2 versus CA1 PNs to glutamate uncaging on proximal and distal spines

The difference in somatic EPSP size evoked by stimulation of the EC inputs in CA2 compared with CA1 PNs could reflect a difference in the size of the EPSP elicited by a single synapse onto a given dendritic spine and/or differences in the total number of EC inputs. To assess the impact of a synaptic response generated at a single distal spine, we performed two-photon glutamate-uncaging at single spines and
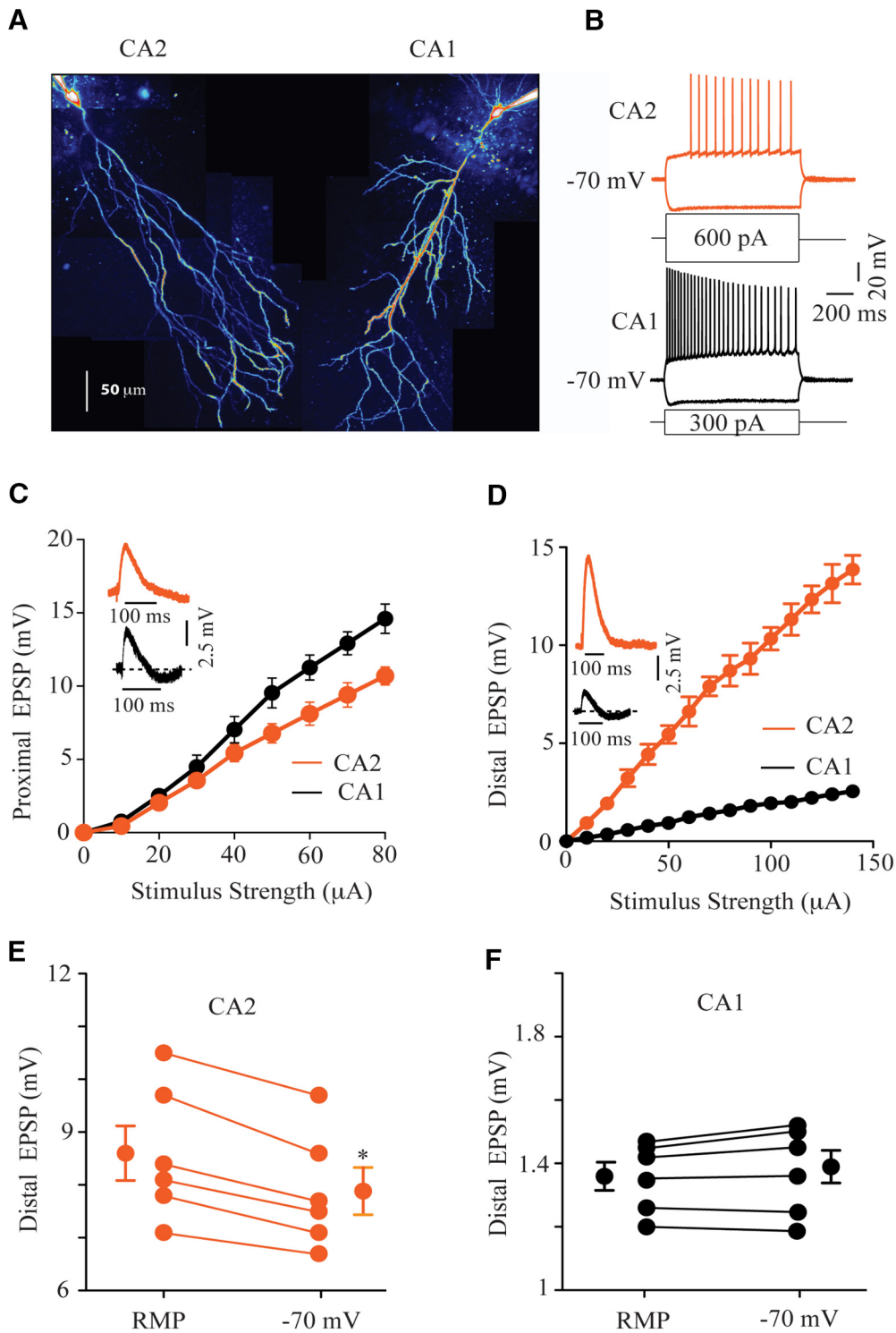
Figure 1. Differential synaptic drive onto CA2 versus CA1 PNs. **A**, Two-photon images of CA2 and CA1 PNs filled with Alexa-594 during whole-cell recordings. **B**, Voltage responses of CA2 and CA1 PNs to 1000 ms depolarizing and hyperpolarizing current steps. **C**, **D**, Mean EPSP input–output curves in CA1 and CA2 PNs obtained during electrical stimulation with electrode placed in proximal (**C**) and distal (**D**) regions of the slice to stimulate Schaffer collateral and EC inputs, respectively. **E**, **F**, Individual and mean distal EPSP amplitudes measured in response to a 70 μA stimulus at the resting membrane potential (RMP) and with the membrane initially held at −70 mV from CA2 and CA1 PNs, respectively. Inset, Representative excitatory synaptic voltage responses. Orange represents CA2 PN. Black represents CA1 PN. GABA receptors were blocked using SR 95531/CGP 55845 during all experiments. Error bars indicate ± SEM. *$p < 0.01$.

measured the uEPSPs at the soma (Fig. 2). Neurons were filled through the patch pipette with AlexaFluor-594 (25 μM) and imaged with two-photon laser scanning microscopy to visualize cellular morphology and identify spines in the proximal (~100 μm from soma) and distal (~350 − 400 μm from soma) dendrites. To ensure a constant delivery of uncaging laser power at individ-

ual spines, we followed a procedure (Bloodgood and Sabatini, 2007) in which the laser intensity was adjusted in each experiment so that a 500 μs light pulse directed to the spine head bleached ~40% of the red fluorescence (which fully recovered within a few hundred milliseconds). The uncaging light spot was then systematically varied around the periphery of a neighboring spine (in the same focal

Table 1. Passive membrane properties and sag amplitudes of CA2 and CA1 PNs[a]

	RMP (mV)	Capacitance (pF)	Input R (MΩ)	Sag amplitude (mV)
CA2 PNs	−75.5 ± 1.6	310.5 ± 26.6	85.5 ± 16.6	3.9 ± 0.6
CA1 PNs	−68.5 ± 1.4*	167.5 ± 17.6**	116.5 ± 15.6*	8.9 ± 0.7**

[a]$n = 8$.

*$p < 0.001$; **$p < 0.0001$; CA2, versus CA1 comparison (unpaired t test).

plane) to determine the location that produced the maximal uEPSP measured at the soma. Only spines that were clearly resolvable at the light microscopic level were chosen for these experiments, primarily stubby and mushroom-shaped spines.

We first measured the somatic uEPSP evoked by glutamate uncaging at spines in the proximal (SR) region of CA1 or CA2 apical dendrites, ~100 μm from the soma. For CA1 PNs, we imaged spines on oblique dendrites in SR; and for CA2, we examined spines on the secondary dendrites within SR at a similar distance from the soma, past the initial branch point. There was no significant difference in the somatic uEPSP amplitude in response to glutamate uncaging at spines located in the proximal regions of CA1 or CA2 dendrites within SR (Fig. 2A,B,E). Thus, the uEPSP amplitude at the soma for CA2 spines was 1.03 ± 0.1 mV compared with 1.1 ± 0.12 mV for CA1 spines ($n = 15$, $p > 0.05$).

In contrast, when we performed glutamate uncaging onto distal spines in SLM (Fig. 2C,D,F), we found that the uEPSP was nearly 2.0-fold larger at the soma of CA2 versus CA1 PNs (Fig. 2C,D,F). As spine responses generally scale with spine size, we grouped spines into two categories, small spines (<0.5 μm apparent diameter) and large spines (>0.5 μm in apparent diameter), using an estimate of spine diameter obtained from AlexaFluor-594 fluorescence images (Fig. 2C). With small-diameter spines, the distally evoked uEPSP measured at the soma in CA2 PNs was 0.28 ± 0.04 mV, whereas the response in CA1 was approximately half the size (0.16 ± 0.03 mV; $n = 30$; $p <$ 0.001) (Fig. 2D,G). The mean amplitude of the uEPSP in response to glutamate uncaging at large spines was also nearly 2.0-fold larger for CA2 (0.55 ± 0.03 mV) versus CA1 (0.29 ± 0.02 mV) PNs ($n = 30$; $p < 0.001$). In addition, the responses at large spines were ~2.0-fold larger than the responses at small spines, for both CA1 and CA2 PNs (Fig. 2D,G). Interestingly, we found a higher percentage of large spines in distal dendrites of CA2 (53 ± 2.4%) compared with CA1 (33 ± 3%) PNs ($n = 6$; $p < 0.001$), which may further contribute to the overall difference in EPSP size.

Role of I_h in differential responses of CA2 versus CA1 PNs to glutamate uncaging on distal spines

What are the mechanisms responsible for the nearly twofold difference in uEPSP size in CA2 compared with CA1 PNs generated by activation of single spines? We first evaluated the potential contribution of the hyperpolarization-activated cation current I_h, which is strongly expressed in the apical dendrites of CA1 PNs, where it acts as a depolarizing shunt conductance to constrain the amplitude of the distally evoked EPSC input (Magee, 1998, 1999; Nolan et al., 2004; George et al., 2009). In CA1 PNs, approximately two-thirds of the total I_h is generated by HCN1 subunits, with the remainder generated by HCN2 subunits (Ludwig et al., 2003; Nolan et al., 2004). Both HCN subunits are strongly expressed in CA1 apical dendrites in a striking gradient of increasing expression with increasing distance from the soma (see also Santoro et al., 1997; Lörincz et al., 2002; Notomi and Shigemoto, 2004) (Fig. 3). The potential role of I_h in regulating dendritic integration in CA2 PNs has not been previously addressed.

We first assessed the potential role of differential I_h levels by examining HCN1/HCN2 subunit expression in CA2 compared with CA1 using immunohistochemistry. Immunolabeling with HCN1- and HCN2-specific monoclonal antibodies revealed that both subunits are highly enriched in the SLM region of CA1 but are expressed at much lower levels in SLM of CA2 (Fig. 3). In the more proximal somatodendritic compartment, including in SR, HCN2 is expressed at approximately similar levels in CA1 and CA2. However, in contrast to the striking increase in HCN2 expression in SLM of CA1, HCN2 is expressed relatively uniformly throughout the radial axis of CA2 (Fig. 3A). Although HCN1 does show a slight enrichment in SLM of CA2 (Fig. 3B), we hypothesized that this signal most likely reflects the known presynaptic expression of HCN1 in the axons and presynaptic terminals of the entorhinal cortex inputs to CA2, which run through SLM (Huang et al., 2012; Wilkars et al., 2012). A perforant path origin of the HCN1 signal in SLM of CA2 is consistent with the similar pattern of enriched HCN1 signal in SLM of CA3 and the molecular layer of DG (Fig. 3B), two regions that contain dense perforant path projections but whose principal neuron soma express little or no HCN1 mRNA (Santoro et al., 2000).

To more specifically address this hypothesis, we took advantage of a mouse line in which the HCN1 and HCN2 auxiliary subunit TRIP8b (Santoro et al., 2004, 2009; Zolles et al., 2009) is deleted. Previous studies found that TRIP8b is necessary for dendritic (Lewis et al., 2011; Piskorowski et al., 2011) but not axonal or presynaptic (Huang et al., 2012) expression of HCN1. Thus, deletion of TRIP8b strongly impairs somatodendritic expression of HCN1 but leaves presynaptic expression of HCN1 intact. By comparing the residual HCN1 labeling in TRIP8b KO mice with the HCN1 labeling in wild-type mice, it is therefore possible to obtain an estimate for dendritic HCN1 expression. As seen in Figure 3B, HCN1 labeling in CA2 SLM is similar in wild-type and TRIP8b knock-out animals, supporting the hypothesis that this signal represents presynaptic labeling of perforant path axons. This is in striking contrast to the dramatic decrease in HCN1 labeling in CA1 SLM of the TRIP8b KO mice, which supports the electrophysiological (Magee, 1998) and electron microscopic (Lörincz et al., 2002) findings that HCN1 is highly enriched in CA1 PN distal dendrites. Finally, as HCN1 and HCN2 assemble efficiently into heteromultimers (Chen et al., 2001), our finding that HCN2 is expressed uniformly throughout the CA2 region in wild-type mice further supports the idea that the enrichment of HCN1 in SLM of CA2 is presynaptic. Based on these results, we conclude that, whereas HCN1 and HCN2 are present in a gradient of increasing density in CA1 apical dendrites, both subunits are expressed at low, uniform levels in CA2 apical dendrites. Results from computer simulations of CA1 and CA2 electrophysiological properties described below further support this conclusion.

Consistent with differences in HCN1 expression, the depolarizing sag in somatic membrane potential elicited by somatic hyperpolarizing current steps, a characteristic feature of I_h activation, was much larger in CA1 compared with CA2 PNs (Fig. 4A,D; Table 1). Moreover, application of the I_h antagonist ZD7288 (10 μM) caused a much greater hyperpolarization of the resting membrane, increase in input resistance, and increase in membrane time constant in CA1 compared with CA2 PNs (Fig. 4B,C,E).

To determine the potential contribution of I_h to regulating EPSP amplitude, we recorded uEPSPs from CA1 and CA2 PNs in the absence and presence of 10 μM ZD7288 (Fig. 4F,G). Blockade of I_h increased the amplitude of the uEPSP by a factor of 1.47 ± 0.13 ($n = 10$; $p < 0.01$) in CA1 PNs, from 0.17 ± 0.02 mV in
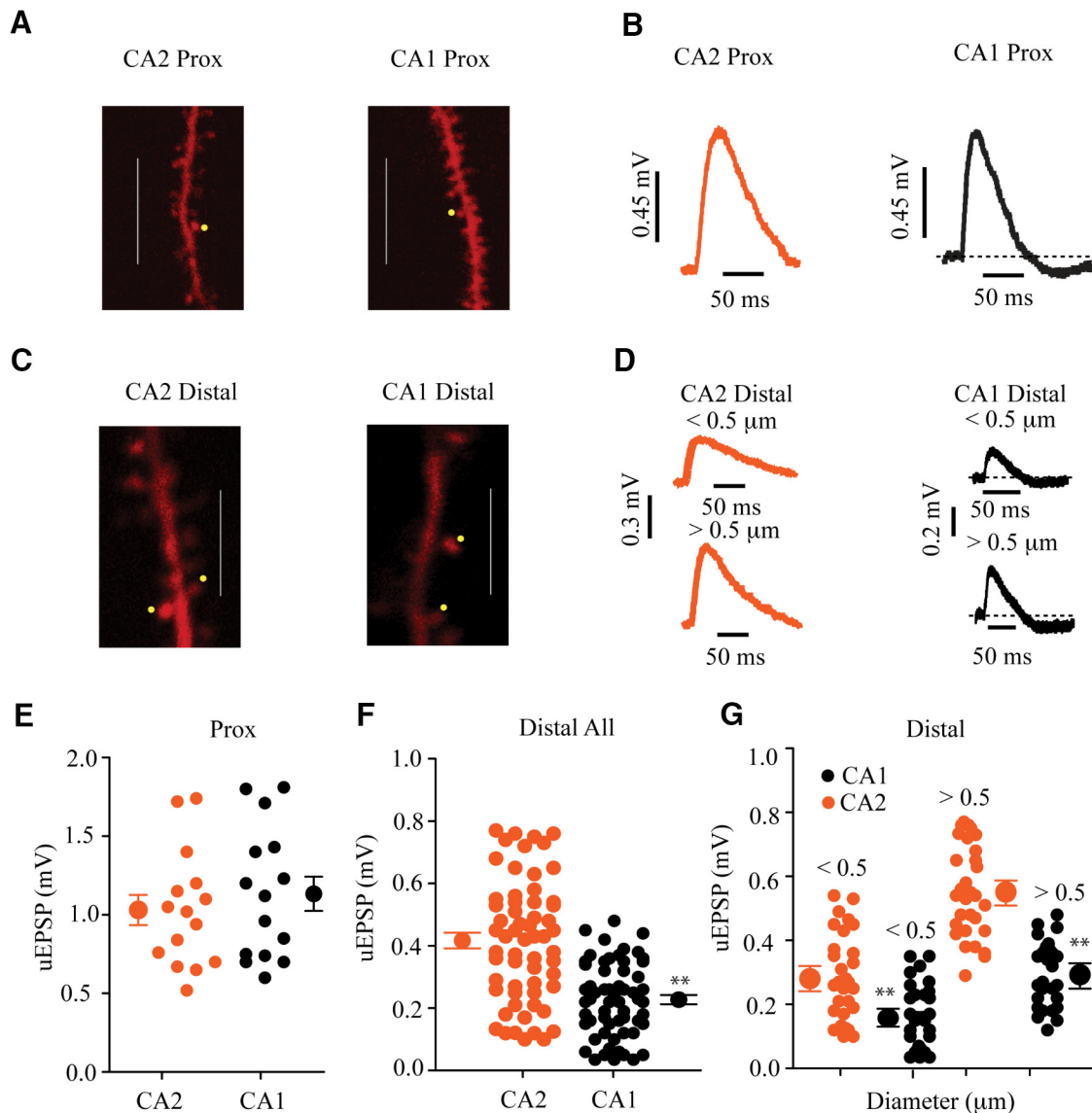
Figure 2. Glutamate uEPSPs in CA2 and CA1 PNs. **A**, **C**, Two-photon laser-scanning microscopy images of Alexa-594 fluorescence showing structure of proximal (**A**) and distal (**C**) spiny apical dendrites of CA2 and CA1 PNs. Yellow dots indicate the location of a 500 μs spot of 725 nm laser light used to trigger 2-photon-mediated photolysis of MNI glutamate. **B**, Representative traces of uEPSPs recorded at the soma evoked by glutamate uncaging at single proximal spines of CA2 (orange) and CA1 (black) PNs. **D**, Representative traces of uEPSPs recorded at the soma in response to glutamate uncaging at single distal small spines (top; <0.5 μm in diameter) or large spines (bottom; >0.5 μm in diameter) of CA2 (orange) and CA1 (black) PNs. **E**, **F**, Individual data and mean somatic uEPSP amplitude evoked by glutamate uncaging at single proximal and distal spines. **G**, Individual data and mean somatic uEPSP amplitude evoked by glutamate uncaging at single distal small spines (<0.5 μm) or large spines (>0.5 μm) of CA2 and CA1 PNs. Error bars indicate $\pm$ SEM. **p < 0.001. Scale bars: **A**, 10 μm; **C**, 5 μm.

control conditions to 0.25 $\pm$ 0.03 mV in the presence of the I_h blocker. In contrast, ZD7288 caused a much smaller (1.18-fold) and statistically insignificant increase in uEPSP size in CA2 PNs (uEPSP = 0.28 $\pm$ 0.03 in absence of ZD7288 vs 0.33 $\pm$ 0.04 mV in the presence of drug; $n = 10$; $p > 0.05$). ZD7288 also reduced the afterhyperpolarization following the EPSP, which was more prominent in CA1 compared with CA2 and which results from the deactivation of I_h during the EPSP depolarization. Thus, differences in dendritic I_h expression can account for approximately half the difference in the distally evoked uEPSP amplitude between CA1 and CA2 PNs.

Small differences in CA2 and CA1 distal spine ultrastructure and AMPAR number
The remaining difference in uEPSP size measured at the soma of CA2 and CA1 PNs with I_h blocked could result from differ-

ences in the passive integrative properties of the dendrites and/or a difference in the number of AMPARs per spine. We therefore determined AMPAR expression using serial section postembedding immunogold electron microscopy on freeze-substituted hippocampal tissue. We also performed a more detailed analysis of spine size because synaptic AMPAR number and, hence, synaptic strength often varies with spine size (e.g., Matsuzaki et al., 2001; Katz et al., 2009). Because CA2 PN dendrites in SLM are embedded in a network of overlapping dendrites from CA1 and CA3 PNs, we used a genetic approach to identify CA2 PN spines. We injected an adeno-associated virus vector-expressing GFP in a Cre recombinase-dependent manner into the CA2 region of adult *Amigo2-Cre* mice, which express Cre (and therefore will express GFP) selectively in CA2 PNs (Hitti and Siegelbaum, 2014). Antibodies linked to different-sized immunogold particles were then used to label

A

B
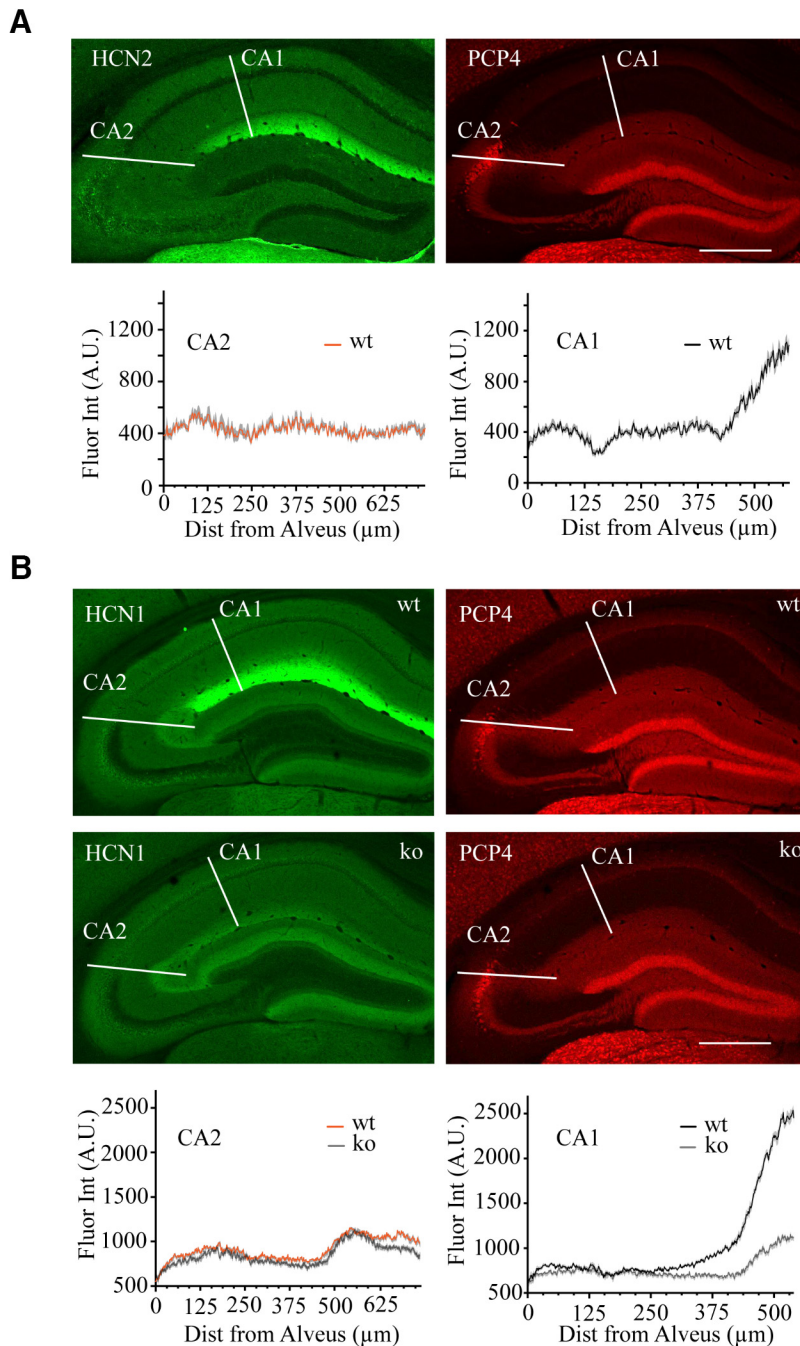
Figure 3. HCN1 and HCN2 immunohistochemistry in hippocampal slices. **A**, Double immunofluorescence labeling for HCN2 (green, left) and the CA2 marker PCP4 (red, right) in hippocampal slices from wild-type mice. Graphs plot HCN2 fluorescent labeling intensity along the lines shown in CA1 and CA2 regions (measurements from $n = 11$ slices obtained from 3 animals). Solid lines indicate mean values. Shaded areas represent $\pm$ SEM. **B**, Double immunofluorescence labeling for HCN1 (green, left panels) and the CA2 marker PCP4 (red, right panels) in hippocampal slices from TRIP8b$^{+/+}$ (wild-type [wt], top panels) and TRIP8b$^{-/-}$ (knock-out [ko], bottom panels) mice. Note the much stronger HCN1 labeling in slices from wt mice in CA1 versus CA2 regions. Graphs represent HCN1 fluorescence intensity along the lines shown in CA1 and CA2 regions in hippocampal slices from wt and ko mice (wt, measurements from $n = 22$ slices from 3 wt animals; ko, measurements from $n = 20$ slices from 3 ko littermates). Measurements from wt and ko slices were normalized to the respective average signal obtained from PCP4 double staining to correct for potential variation in absolute intensity values. All stainings were performed on coronal brain slices, collected at bregma -1.8 mm. Scale bars, 500 μm.

GFP and AMPARs in slices obtained 2–3 weeks after viral injection, enabling us to measure AMPAR expression specifically in CA2 PN spines (Fig. 5A–C). CA1 PN spines were identified unambiguously using tissue obtained from the SLM layer in the mid-region of CA1 along the transverse axis, far

from the CA2 and subicular borders (Fig. 5D–F). The mean number of AMPAR particles located to synapses (within 20 nm of a postsynaptic density) per spine averaged over all spines was ~25% greater (Fig. 5I) in CA2 (4.3 ± 0.3; $n = 301$) than CA1 (3.4 ± 0.3; $n = 143$; $p < 0.05$).

Three-dimensional reconstructions of distal dendritic segments of CA1 and CA2 PNs (Fig. 5A–F) were used to measure synaptic AMPAR expression as a function of spine volume in a large population of distal spines. There was a strong correlation between spine volume and synaptic AMPAR particle number in spines from both CA1 and CA2 PNs (Fig. 5G). A cumulative plot of the distribution of spine volume (Fig. 5H) shows a significantly different distribution (Kolmogorov–Smirnov test: $p < 0.0001$). Smaller spines (defined as those with volume < 0.05 μm^3) have a 50% larger mean volume in CA2 (0.024 ± 0.0007 μm^3, $n = 249$) versus CA1 (0.016 ± 0.001 μm^3, $n = 123$; $p < 0.0001$), whereas larger spines (volume > 0.05 μm^3) have a slightly smaller volume in CA2 (0.085 ± 0.005 μm^3, $n = 52$) compared with CA1 (0.107 ± 0.009 μm^3, $n = 20$; $p < 0.05$). However, there was no significant difference in mean volume for the total population of spines in CA2 (0.034 ± 0.002 μm^3, $n = 301$) compared with CA1 (0.029 ± 0.003 μm^3, $n = 143$; $p > 0.05$).

Spines can differ as to whether they contain nonperforated or perforated synapses, the latter having a PSD with at least one discontinuity when viewed in serial electron microscopy sections (Geinisman, 1993; Ganeshina et al., 2004). Because perforated synapses express a higher number of AMPARs than nonperforated synapses (Kharazia and Weinberg, 1999; Ganeshina et al., 2004; Nicholson and Geinisman, 2009), an increased fraction of perforated synapses could contribute, in principle, to the larger distally evoked EPSP in CA2 versus CA1 PNs. However, we found that the percentage of spines with perforated synapses was actually greater in CA1 than in CA2, for both small spines (52.4% in CA1 vs 31.8% in CA2) and large spines (100% in CA1 vs 85% in CA2). These results indicate that spine and synapse ultrastructure and AMPAR expression are relatively similar in the SLM region in CA2 and CA1 and so may not be a major determinant of differences in EPSP size.

Differences in spine number and dendritic morphology between CA2 and CA1 PNs

The above analysis suggests that differences in Ih expression and AMPAR number may account for part, but perhaps not all, of the
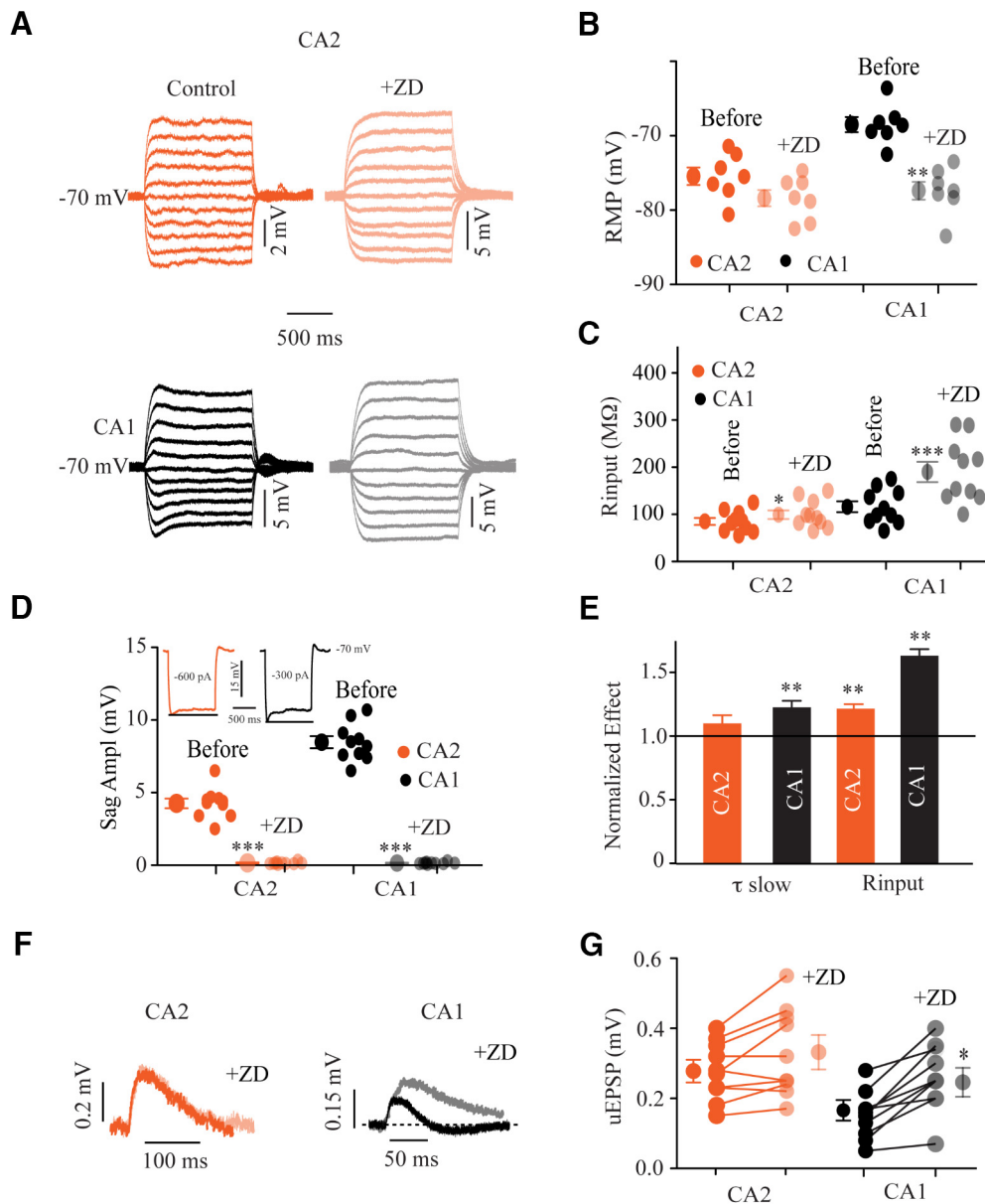
Figure 4. Effect of I_h on passive membrane properties and distal uEPSP of CA2 and CA1 PNs. **A**, Representative traces of membrane responses measured from soma of CA2 (orange) and CA1 (black) PNs to depolarizing and hyperpolarizing current injections in normal ACSF and during application of 10 μм ZD7288. **B**, Mean changes in resting membrane potential before and after wash-in of ZD7288. **C**, Summary of mean values of input resistance (R_{input}) measured from CA1 (black) and CA2 PNs (orange), in normal ACSF and during application of 10 μм ZD7288. **D**, Mean changes in sag amplitude before and after wash-in of ZD7288. Insets, Membrane depolarizing "sag" responses characteristic of I_h upon hyperpolarizing current injections in CA2 (orange) and CA1 (black) PNs. **E**, Bar plots of normalized effect of 10 μм ZD7288 on slow membrane time constant and input resistance, normalized to values obtained in ACSF. **F**, Representative somatic uEPSPs evoked by glutamate uncaging at a single distal spine of CA1 (black) and CA2 (orange) PNs, before and during application of 10 μм ZD7288 (light colored traces). **G**, Individual and mean uEPSP amplitude before and after application of ZD7288. Error bars indicate ± SEM. *$p < 0.01$. **$p < 0.001$. ***$p < 0.0001$.

~2.0-fold difference in the somatic voltage response to the activation of a single spine in CA2 compared with CA1 PNs. Moreover, the difference in uEPSP size is much less than the 5- to 6-fold difference in EPSP size in these neurons evoked by electrical stimulation of the distal inputs. We therefore next assessed whether differences in dendritic morphology and/or synapse number may also contribute to differences in the uEPSP and electrically evoked compound EPSP between CA2 and CA1 PNs. We therefore performed a detailed analysis of dendritic morphology and spine number in the distal dendrites for the two classes of neurons, with the number of spines providing an approximate measure of the number of excitatory synaptic inputs. Individual CA1 and CA2 PNs were filled with biocytin (1%) during patch-

clamp recordings, and 3D reconstructions of dendritic morphology were performed in fixed hippocampal slices after visualizing the neurons with DAB (Fig. 6*A*,*B*). A previous study from our laboratory examined the role of differences in dendritic branch geometry in dendritic spike propagation but did not examine spine number or dendritic branch diameter (Sun et al., 2014).

To estimate the number of excitatory synaptic inputs, we counted the number of spines in both proximal and distal dendrites of CA2 and CA1 PNs. We found that the number of spines on distal dendrites of CA2 PNs (6308 ± 272.4) was 3.5 ± 0.4-fold greater than that of CA1 PNs (1735 ± 165.6; $n = 9$; $p < 0.0001$; Fig. 6*C*). The higher CA2 spine number resulted from two factors. First, the total length of CA2 dendrites in SLM (2755 ±
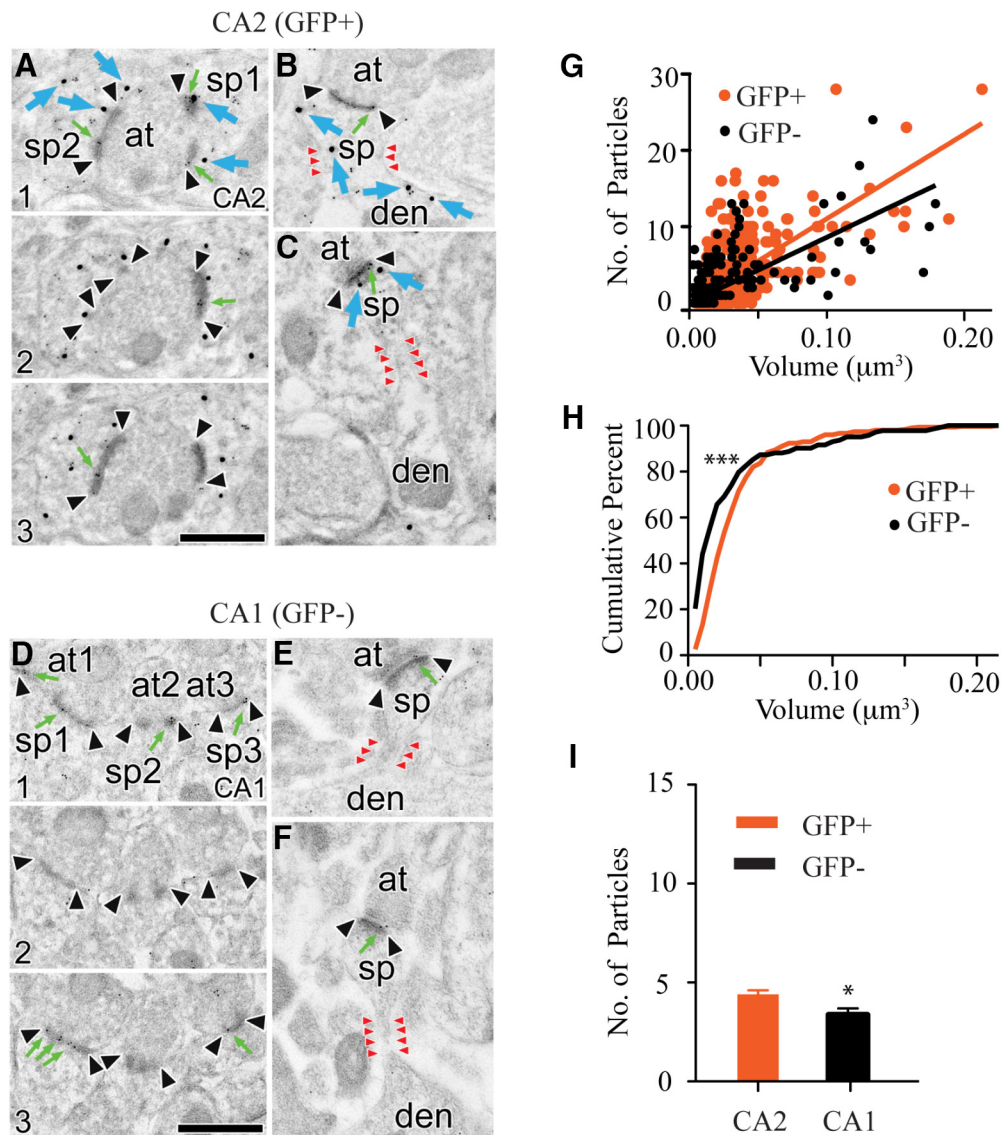
Figure 5. Electron micrographs of GFP-expressing CA2 and GFP-negative CA1 distal synapses. **A**, Electron micrographs of three serial sections (1–3) through two GFP-positive (CA2) and AMPAR-positive synapses in SLM. Arrowheads indicate the borders of the PSD. Green arrows indicate clusters of immunogold particles for AMPARs projected onto the PSD. Blue arrows indicate large, 25 nm immunogold particles for GFP (CA2 marker). sp, Spine; at, axon terminal. **B**, **C**, Single section electron micrographs capturing the spine neck (red arrowheads) attachment to parent dendrite (den). **D**, Same as in **A**, but for synapses in CA1 SLM. Note the absence of GFP-immunogold particles. **E**, **F**, Single section electron micrographs for synapses in CA1 SLM (conditions and labels as in **B**,**C**). Scale bars, 500 nm. **G**, Correlation between spine volume and AMPAR particle number in the postsynaptic density for all GFP-positive (CA2: $r = 0.59$) and GFP-negative (CA1: $r = 0.6$) distal spines. **H**, Percentage cumulative distribution plots of spine volume for all GFP-positive (CA2) and GFP-negative (CA1) spines (Kolmogorov–Smirnov test: $p < 0.0001$). **I**, Mean number of AMPA receptor particles in the postsynaptic density in total spine population in distal dendrites of CA2 (GFP-positive) and CA1 (GFP-negative) PNs. Error bars indicate $\pm$ SEM. *$p < 0.05$. ***$p < 0.0001$.

137 μm) was 67 $\pm$ 1.7% larger ($n = 5$; $p < 0.001$) than the length of CA1 dendrites in SLM (1850 $\pm$ 130 μm). Second, the density of spines in SLM of CA2 (2.3 $\pm$ 0.11 spines/μm) was 2.4 $\pm$ 0.3-fold higher ($n = 9$; $p < 0.001$) than SLM spine density in CA1 (0.99 $\pm$ 0.13 spines/μm). In contrast, the spine density was significantly higher on the proximal dendrites of CA1 PNs (3.8 $\pm$ 0.2 spines/μm) compared with CA2 PNs (2.6 $\pm$ 0.3 spines/μm; $p < 0.001$), consistent with the larger EPSP evoked by proximal stimulation in CA1 compared with CA2 PNs (Fig. 1C).

We extended our previous morphological analyses (Sun et al., 2014) by determining differences in soma and dendrite size, using a separate set of filled neurons ($n = 5$). First, we found that the CA2 PN soma is much larger than that of CA1 PNs (surface area of 403 $\pm$ 20 μm^2 in CA2 vs 164 $\pm$ 25 μm^2 in

CA1; $n = 5$; $p < 0.0001$). Within SLM, CA2 PNs have a greater total dendrite length, surface area, volume, and dendritic diameter (Fig. 6C,D).

Our analysis also confirmed the differences in dendrite branching described by Sun et al. (2014). Thus, CA1 PNs typically extend a single primary apical dendrite that reaches the border of SLM, where it radiates into a number of thin tufted dendrites within SLM. Within SR, the main apical dendrite gives rise to numerous oblique dendrites. In contrast, in all CA2 PNs, the primary apical dendrite divides into several secondary branches relatively close to the soma ($\sim$30–100 μm). These secondary branches extend to the distal regions of SLM and give rise to very few oblique branches in SR. These results were quantified using a Sholl analysis, which confirmed that CA2 PNs have significantly fewer oblique branches in SR but more branches in SLM com-
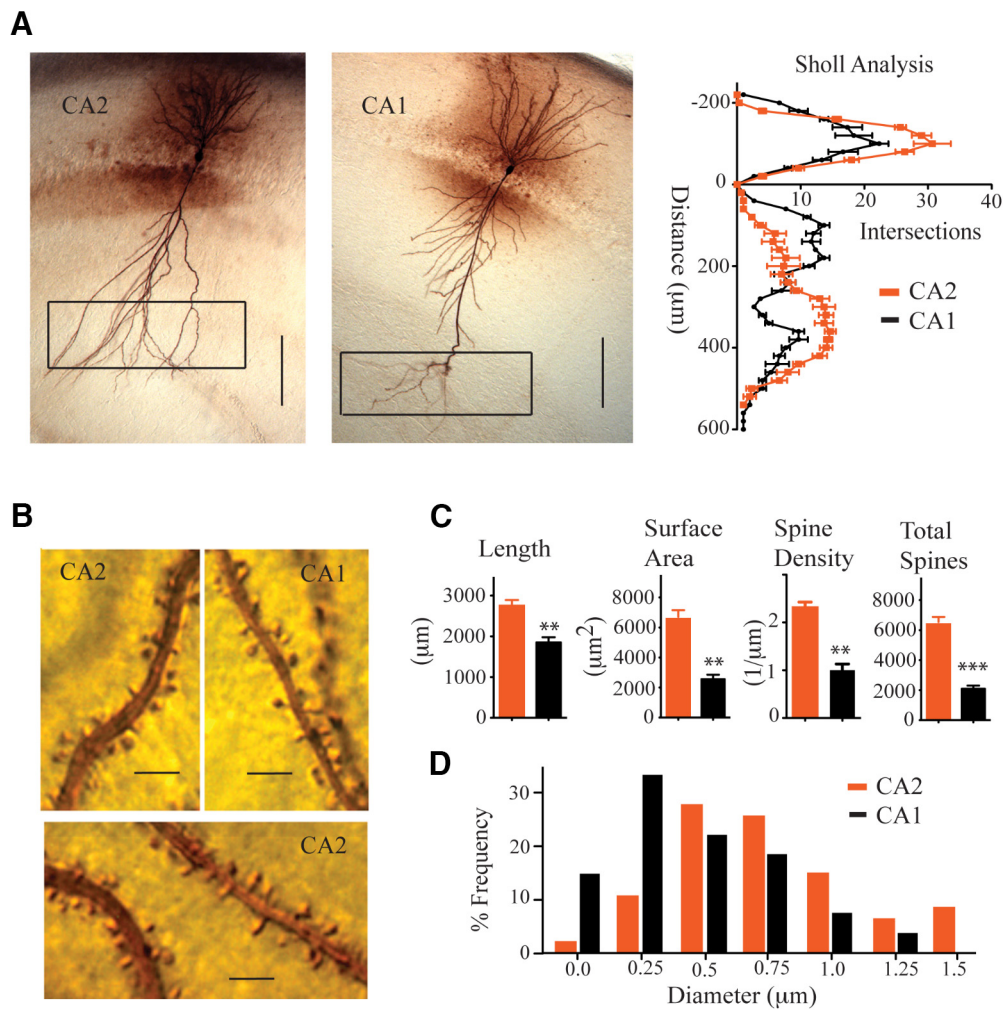
Figure 6. Morphological features of CA2 and CA1 PNs. ***A***, Light microscopic images of biocytin-filled CA2 and CA1 PNs (left) and Sholl analysis of CA2 (orange) and CA1 (black) dendritic branching (right). Boxes represent distal dendritic regions in SLM. ***B***, High-magnification images of distal dendrites (>350 μm from soma) and spines of CA2 and CA1 PNs. ***C***, Mean dendrite total length, surface area, spine density, and number for distal dendrites of CA2 and CA1 PNs. ***D***, Frequency distribution of distal dendrite diameter for CA2 and CA1 PNs. Error bars indicate ± SEM. **$p <$ 0.001. ***$p <$ 0.0001. Scale bars: ***A***, 150 μm; ***C***, 5 μm.

pared with CA1 PNs (Fig. 6A). The larger and less branched dendrites of CA2 PNs may facilitate the propagation of the distal EPSP to the soma compared with propagation along CA1 PN dendrites, and thereby contribute to the 2.0-fold difference in single spine responses. We used computer simulations below to address this possibility.

Multicompartmental membrane models with I_h
As the number of AMPARs are approximately equivalent between CA1 and CA2 PN dendrites, the 2.0-fold larger uEPSP at the soma of CA2 PNs compared with CA1 PNs may result from either a greater local dendritic depolarization in response to a single spine input and/or an enhanced dendritic propagation of the local EPSP to the soma. Because the small size of the distal dendrites precludes direct recordings of the local distal EPSP, we performed multicompartmental computer simulations in the NEURON simulation environment (Hines and Carnevale, 1997) based on the morphological reconstructions of CA1 and CA2 PNs from biocytin fills (Fig. 7A) and our electrophysiological results.

We first constructed a purely passive model based, simulating conditions where I_h was blocked, using values for specific membrane resistance (R_m), internal resistivity (R_i), and capacitance

(C_m) from published results (Jarsky et al., 2005; Harnett et al., 2012). When we did not include the contribution of dendritic spines to total surface area, the predicted input resistance (R_{Input}) values for CA1 and CA2 PNs were several-fold larger than our experimental results (Fig. 7B,D). To incorporate spines, we divided R_m and multiplied C_m in a region-dependent manner by scaling factors for spine surface membrane area (Table 2) calculated from our measured spine densities, dendritic diameters, and previously reported spine surface area measurements (Harris and Stevens, 1989). After including the spine scaling factors, the R_{Input} values closely matched the experimental values for both CA1 and CA2 PNs, indicating that the chosen standard values of R_m and R_i were appropriate for both types of neurons.

Next, we extended the passive model by incorporating I_h. In CA1 PNs, the I_h conductance was distributed in a linear gradient of increasing density in the apical dendrites as a function of distance from the soma, based on immunohistochemical (see also Santoro et al., 1997; Lörincz et al., 2002) (Fig. 3) and electrophysiological results (Magee, 1998). In contrast, for CA2 PNs, I_h conductance was distributed uniformly throughout the dendritic tree, consistent with our immunohistochemical results (Fig. 3). The I_h conductance values in both CA1 and CA2 models
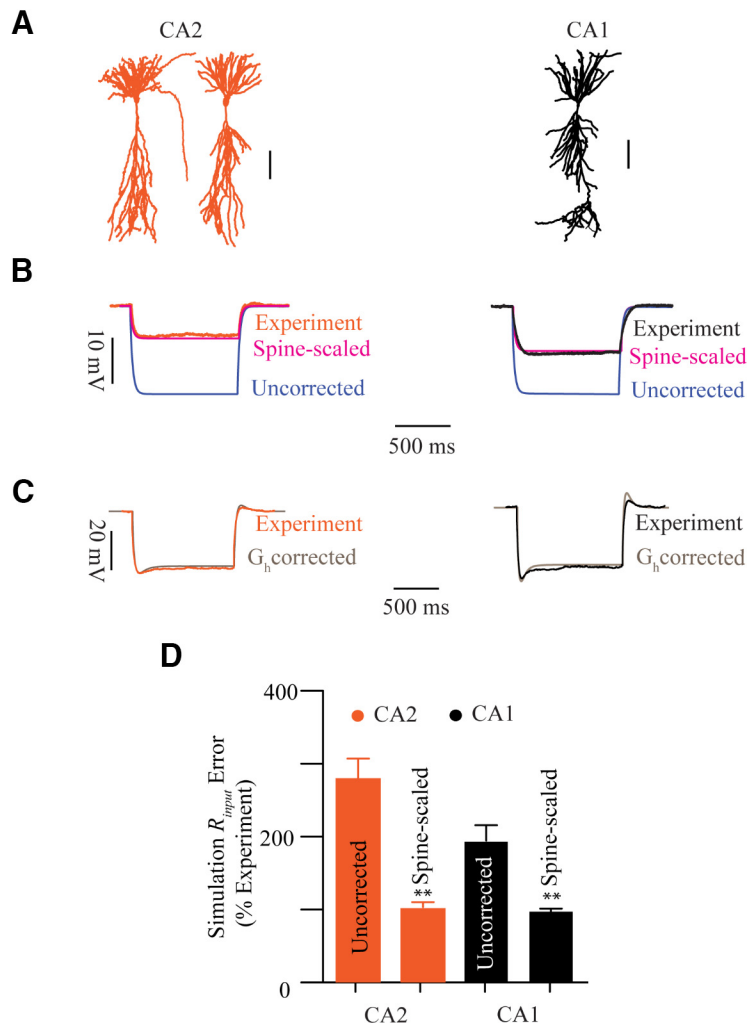
Figure 7. Simulations of voltage response to hyperpolarizing current steps from morphologically based NEURON models incorporating passive membrane properties, I_h, and spinescale corrections. **A**, Representative reconstructed CA1 and CA2 PNs. **B**, Simulated voltage responses to hyperpolarizing current step in the absence of I_h, with (pink) or without (orange) correction for spine membrane area for model CA1 (left) and CA2 (right) PNs, compared with experimental voltage responses. Orange represents CA2. Black represents CA1. **C**, Comparison of simulated voltage responses in the presence of I_h (orange) to experimental data from CA1 (left, black) and CA2 (right, orange) PNs. **D**, Percentage error in calculated versus experimental input resistance (R_{input}) for CA1 and CA2 PNs, before and after correction for spines. Error bars indicate ± SEM. **$p < 0.001$.

Table 2. Spine scaling factors for dendrites of CA2 and CA1 PNs

Segment	CA1 PNs	CA2 PNs
SR thick/proximal	1.74	1.78
SR thick/distal	1.78	1.86
SR thin	2.72	2.45
SLM medium	1.72	2.88
SLM thin	1.63	2.96

were adjusted so that the computed somatic sag amplitude (steady-state − peak voltage during hyperpolarizing current step) matched our experimental values (Fig. 7C). Inclusion of I_h caused a positive shift in the resting potential of 3.3 ± 0.3 mV and 8.5 ± 0.4 mV in CA2 and CA1 PNs, respectively, in excellent agreement with our experimental observations (2.94 ± 0.4 mV and 8.9 ± 2 mV shift in CA2 and CA1, respectively; Fig. 4B).

Simulation of responses to single spine inputs in CA2 and CA1 PNs

We next used our computational models to explore the dendritic and somatic responses to single spine inputs (Fig. 8). The ampli-

tude of the subthreshold EPSP in both CA1 and CA2 PNs is largely determined by the AMPAR conductance, as NMDAR blockade decreases the EPSP amplitude by <20% (Sun et al., 2014). We therefore modeled the kinetics of excitatory synaptic conductances using a two-exponential function appropriate for AMPAR-mediated EPSCs, as previously described (Jarsky et al., 2005). Inclusion of NMDARs did not alter the conclusions from the simulations (data not shown).

Uncaging EPSPs were generated by activating identical AMPAR conductances in individual spines in distal dendrites of CA1 and CA2 PNs. We used a spine neck resistance of 500 MΩ (Harnett et al., 2012), with identical values of spine head and neck parameters used in CA1 and CA2 simulations ($n = 4$ reconstructed CA2 PNs and $n = 3$ CA1 PNs). For each cell, we repeated the uEPSP measurements on a total of 50 spines randomly placed throughout the distal dendritic arbor, with each spine located ~400 μm from the soma (Fig. 8A). We then averaged the 50 spine responses at a given location along the somatodendritic compartment.

We first adjusted the value of the AMPAR conductance in CA2 spines so that the computed somatic EPSP amplitude matched the uEPSP amplitude recorded experimentally, and then used this value for all subsequent CA2 and CA1 simulations. The EPSP was calculated in the head of the activated distal spine, at various positions in the dendritic shaft as the EPSP propagated to the soma, and in the soma itself (Fig. 8B,C).

Activating the AMPAR conductance on a distal spine produced a large EPSP of identical amplitude (45 mV) within the CA2 (44.9 ± 0.7 mV) or CA1 (44.9 ± 0.7 mV) spine head (Fig. 8D,E). In the distal dendritic shaft, immediately under the activated spine, the local depolarization was actually 50% larger in CA1 (31.1 ± 1.2 mV; $n = 150$ spines) than in CA2 (20.7 ± 0.95 mV; $n = 200$ spines; $p < 0.001$), as a result of the higher input resistance of the smaller-diameter CA1 distal dendrites. In contrast, the EPSP values at the soma were reversed: the simulated somatic EPSP in CA2 PNs (0.25 ± 0.01 mV; $n = 200$ spines) was 1.8-fold larger than the CA1 EPSP (0.14 ± 0.01 mV; $n = 150$ spines; $p < 0.001$) (Fig. 8D,E). This CA2/CA1 EPSP ratio is very similar to the ratio of 1.75 for the experimentally determined uEPSPs (Fig. 2).

A comparison of EPSP size in the distal dendritic shaft under the activated spine to the EPSP amplitude measured in the soma revealed that CA1 dendrites produced a 2.6-fold greater attenuation ($p < 0.001$) of the EPSP compared with CA2 dendrites. Thus, the dendritic attenuation factor (ratio of distal to somatic EPSP) was 218 ± 25 ($n = 3$) in CA1 PNs compared with 84 ± 15 ($n = 4$) in CA2 PNs (Fig. 8F,G). Of particular interest, the computed EPSP at the CA1 soma closely matched the CA1 uEPSP amplitude recorded experimentally, supporting the validity of both models.
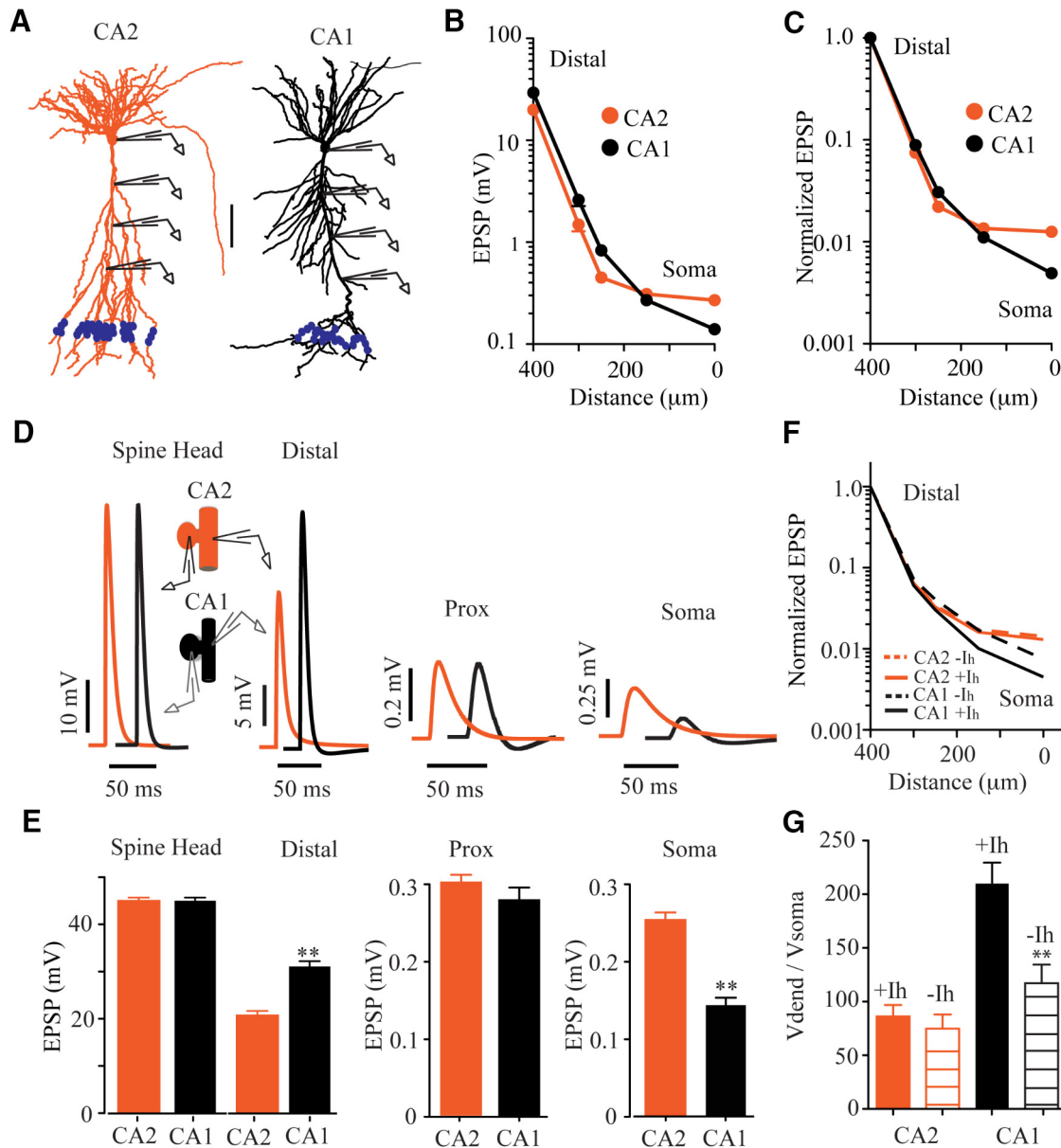
Figure 8. Dendritic integration and propagation of distally evoked EPSPs at single spines in morphologically reconstructed simulations of CA2 (orange) and CA1 (black) PNs. **A**, Representative reconstructions of CA2 and CA1 PNs with synapse locations (dots). Electrodes indicate simulated recording sites. **B**, Log-linear plot of EPSP amplitude as a function of dendritic distance from soma for CA2 and CA1 PNs. **C**, Log-linear plot of normalized EPSP amplitude along dendrite. **D**, Simulated EPSPs generated by AMPAR conductance in a single CA2 and CA1 distal spine (inset) in spine head, distal dendritic shaft just under the spine, at proximal dendrite, and at soma. **E**, Bar graphs represent mean EPSP in distal dendrite spine head, shaft, proximal dendrite, and soma. **F**, EPSP attenuation. The EPSP amplitude in the dendritic shaft at the site of synaptic input (Vdend) was divided by the local propagated EPSP amplitude at a given distance from the synaptic input (Vlocal) and plotted as a function of the distance. Plots represent EPSP attenuation for CA2 (orange) and CA1 (black) in the absence (dashed lines) or presence (solid lines) of simulated I_h. **G**, Bar graphs represent mean voltage attenuation of the distal dendritic EPSP measured at soma in the absence (dashed lines) or presence (solid lines) of simulated I_h. Error bars indicate ± SEM. ******$p < 0.001$.

Removal of I_h from the simulations (Fig. 8 F, G) produced a significant 1.8-fold decrease in the magnitude of dendritic attenuation in CA1 (from 218 ± 25 to 120 ± 23; $n = 3$ cells; $p < 0.001$), prolonged the EPSP decay time course, and eliminated the afterhyperpolarization, consistent with our experimental results (Fig. 4F). In contrast, removal of I_h in the CA2 model produced only a small, 1.15-fold decrease in dendritic attenuation (from 84 ± 15 to 73 ± 14; $n = 4$ cells; $p > 0.05$) and had little effect on EPSP decay, as observed experimentally (Fig. 4F). Removal of I_h enhanced the somatic uEPSP by a factor of 1.2 for CA2 compared with a factor of 1.51 for CA1. These results are

in excellent quantitative agreement with our experimental results showing that blockade of I_h with ZD7288 caused a 1.18-fold increase in the uEPSP in the CA2 PN soma compared with a 1.47-fold increase in the CA1 PN soma (Fig. 4 F, G). In contrast, when we repeated the CA2 simulations with I_h present in a gradient of increasing dendritic expression (with somatic I_h levels adjusted to match our experimental somatic sag amplitude), removal of I_h enhanced the EPSP amplitude by a factor of 1.36, nearly 1.2-fold greater than our experimental value. Thus, the simulation results support the immunohistochemical data (Fig. 3) suggesting that I_h is distributed uniformly in CA2 dendrites.
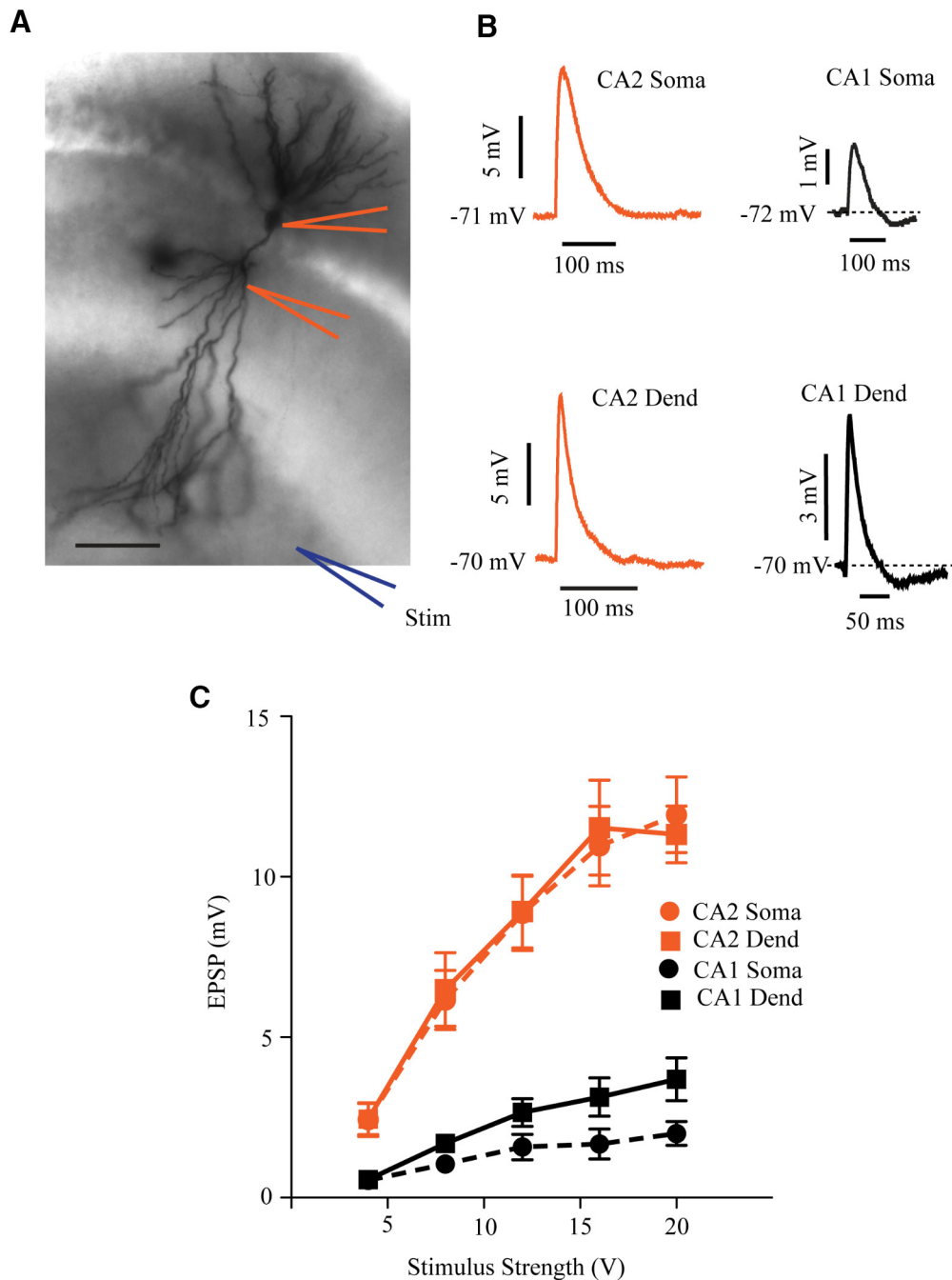
Figure 9. Comparison of experimental input–output curves for EPSPs evoked by distal synaptic stimulation recorded separately from soma and dendrites of CA2 and CA1 PNs. ***A***, Experimental setup. Biocytin filled CA2 PN. The orange electrodes indicate somatic and proximal dendritic recording sites (mean recording sites in CA2 and CA1 PNs are 133 and 173 μm from soma, respectively), and placement of blue stimulating electrode. ***B***, Representative EPSPs at soma and proximal dendrite of CA2 and CA1 PNs. ***C***, Mean somatic and dendritic EPSP input–output curves for CA2 and CA1 PNs. GABA receptors were blocked using SR 95531/CGP 55845 during all experiments. Error bars indicate ± SEM.

One interesting result from the plot of EPSP size versus dendritic distance from the soma was that the major difference in dendritic attenuation between CA1 and CA2 occurred in the more proximal regions of the dendrites in SR, starting 250 μm from the soma. As the EPSP propagated from this point to the soma, the CA1 dendrites produced a 3.0-fold greater attenuation than did the CA2 dendrites (Fig. 8 *B*, *C*). Part of this difference is accounted for by I_h, as the removal of I_h from the simulations greatly decreased the attenuation by the proximal dendrites (Fig. 8*F*). The remaining difference in dendritic attenuation is likely due to the more numerous proximal oblique CA1 dendrites,

which act to shunt the current from the primary CA1 apical dendrite.

Direct dendritic recordings support differential dendritic attenuation of EPSPs

To test the prediction of the model that CA1 proximal dendrites produce a greater attenuation of the EPSP compared with CA2 dendrites, we performed dendritic recordings from more proximal regions of CA2 and CA1 dendrites in the middle of the SR layer, ~150 μm from the soma (Fig. 9). There was remarkably little attenuation of the EPSP as it propagated from this location

to the soma in CA2 dendrites, with nearly identical EPSP input–output relations measured in the proximal dendrites and soma. In contrast, for CA1 PNs, the dendritic EPSP was almost 2.0-fold larger than the somatic EPSP. Thus, the ratio of the EPSP amplitude measured at the proximal dendrite ($\sim$150 μm from the soma) to the somatic EPSP amplitude was equal to 1.02 $\pm$ 0.023 ($n = 7$) in CA2 PNs compared with 1.76 $\pm$ 0.65 ($n = 7$) in CA1 PNs. These experimental results were in remarkably good agreement with our simulations, where the dendritic to somatic EPSP ratio was 1.08 $\pm$ 0.024 ($n = 4$) in CA2 compared with 1.82 $\pm$ 0.06 ($n = 3$) in CA1.

Simulations reveal a differential effect of distal synapse number on somatic EPSPs in CA2 compared with CA1 PNs

The $\sim$2.0-fold larger somatic response to synaptic activation of a single spine in the distal dendrites of CA2 compared with CA1 PNs seen in our experimental and computational results cannot, by itself, account for the 5- to 6-fold difference in the size of the somatic EPSP evoked by distal electrical stimulation. However, given our finding that CA2 distal dendrites have three times as many spines as CA1 distal dendrites (Fig. 6C), we next performed a set of simulations to determine whether a combination of differences in dendritic morphology, I_h expression, and distal synapse number can explain more fully the difference in EPSP size.

We distributed 1000 excitatory synapses with fixed and identical AMPAR conductance (as above) across the distal dendritic arbor in both CA1 and CA2 PN models using the same I_h values used in the single spine simulations. We then computed the relation between somatic EPSP amplitude and the number of spines that were simultaneously activated at random sites throughout the distal dendritic arbor (Fig. 10A). For both CA1 and CA2 PNs, the somatic EPSP amplitude initially increased linearly as a function of the number of activated spines; however, with large numbers of activated spines, the relation became sublinear (Fig. 10B). The sublinearity occurs as enough synapses become activated so that the distal dendritic voltage begins to approach the AMPAR reversal potential (Fig. 10C,D). Of note, the region of sublinearity was reached when many fewer spines were activated in CA1 compared with CA2. Thus, whereas the CA1 EPSP approached a saturating value after activation of $\sim$200 synapses, the CA2 EPSP failed to saturate with even 600 activated synapses. This difference can be largely attributed to the lower input resistance of the large caliber CA2 distal dendrites, which reduces the size of the distal EPSP compared with that in CA1 (Fig. 10B,D).
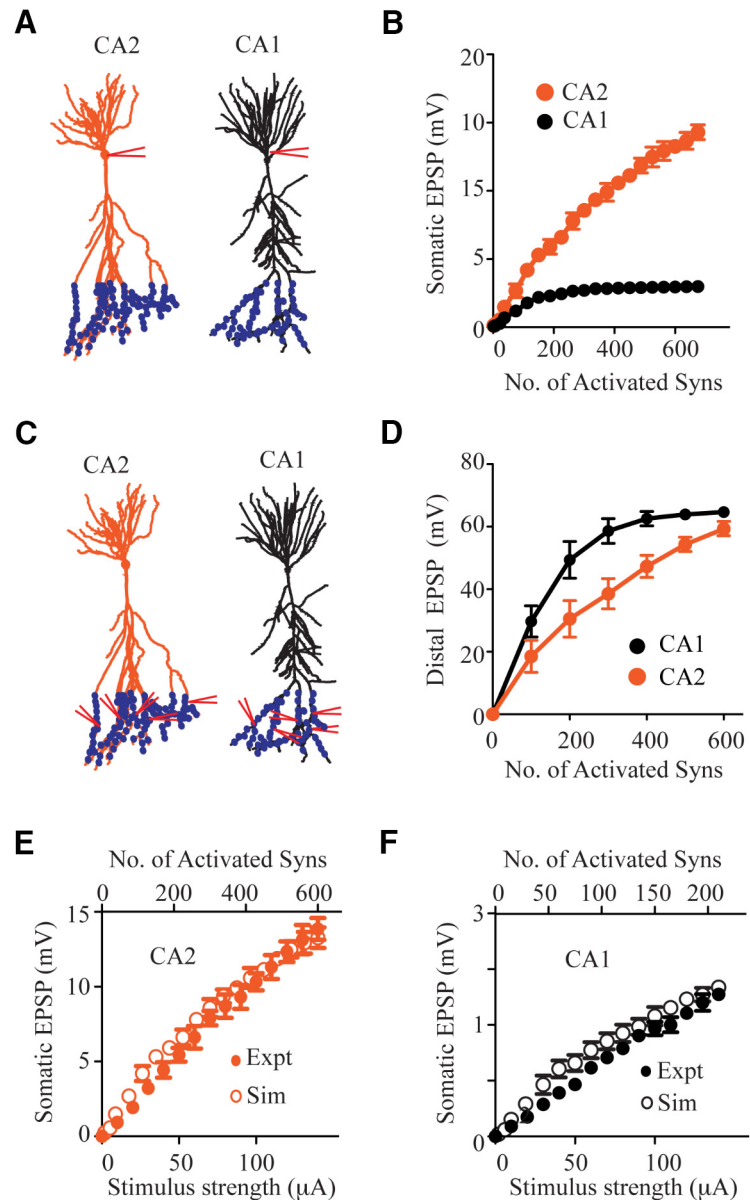
Figure 10. Somatic and local distal dendritic EPSP input–output relation for CA2 and CA1 PNs. **A**, Simulation setup for determining relationship between somatic EPSP amplitude and number of activated distal synaptic inputs for CA2 and CA1 PNs. Blue dots indicate location of synapses randomly distributed in distal dendrites. Electrode, somatic recording site. **B**, EPSP amplitude as a function of number of activated synapses for CA2 and CA1 PNs. **C**, Simulation setup for determining relationship between local distal dendritic EPSP amplitude and number of activated distal synaptic inputs for CA2 and CA1 PNs. Blue dots indicate location of synapses. Electrodes, dendritic recording sites. **D**, Local distal dendritic EPSP amplitude as a function of number of activated synapses for CA2 and CA1 PNs. **E**, **F**, Comparison of experimental EPSP input–output relations (filled symbols) with results from simulations (open symbols) for CA2 (**E**) and CA1 (**F**) PNs. Each comparison had one free scaling parameter, f, that converted stimulus current to number of activated synapses. For CA1, $f = 1.5$ synapses per μA; for CA2, $f = 4.3$ synapses per μA. Error bars indicate $\pm$ SEM.

As a result of the difference in EPSP saturation, the CA2/CA1 EPSP ratio increased linearly as a function of synapse number, from a minimum value of 2.5 with only a few active synapses to a value of $\sim$4.5 with 600 active synapses. Our simulations provided a very good match to our experimentally observed EPSP input–output relations for both CA1 and CA2 PNs (Fig. 10E,F), when we used a single free parameter to convert a unit of stimulating current to the number of activated synapses. Of particular interest, the conversion factor for CA2 was 2.9-fold greater than that for CA1, consistent with the 3.0-fold greater spine density in CA2. Such agreement with experimental results provides a very strong validation of our computational results.

Discussion

Previous studies demonstrated the importance of passive and active dendritic properties in the local integration of synaptic inputs and the propagation of synaptic potentials to the soma (London and Häusser, 2005; Stiefel and Sejnowski, 2007; Stuart and Spruston, 2015). Here, we have extended this analysis by showing that the synergistic interaction of dendritic and synaptic properties determines the distinct responses of CA1 and CA2 PNs to their entorhinal cortex inputs.

Our experimental and computational results indicate that three factors (dendritic morphology, dendritic I_h and synapse number) account quantitatively for the 5- to 6-fold greater somatic EPSP evoked by activation of the distal cortical inputs in CA2 compared with CA1 PNs. The combined differences in dendritic morphology and I_h alone account for the nearly 2.0-fold difference in the amplitude of the somatic EPSP evoked by activation of the AMPA receptors on a single distal spine, with individual differences in I_h and morphology contributing approximately equally. The remainder of the difference in EPSP size evoked by synaptic stimulation results from the 3.0-fold greater number of synapses on CA2 compared with CA1 distal dendrites.

Dendritic morphologies vary widely among different classes of neurons and have been found to greatly influence their information-processing properties (Mainen and Sejnowski, 1996; London and Häusser, 2005; Stiefel and Sejnowski, 2007). Our anatomical results, along with those from a previous study from our laboratory (Sun et al., 2014), pinpoint several key differences in the architecture of CA2 compared with CA1 dendrites. Whereas most CA1 PNs extend a primary dendrite to SLM where it fans out into a fine tuft of thin dendrites, the majority of CA2 PNs have a primary apical dendrite that branches within 100 μm of the soma, sending multiple secondary dendritic branches that extend to SLM. Moreover, CA2 dendrites are more heavily branched in SLM compared with CA1 dendrites, whereas CA1 PNs have many more oblique secondary dendrites in SR that serve to shunt the distal synaptic current as it propagates to the soma. At the same time, the more extensive branching of CA2 distal dendrites and their greater overall length allow for more EC synaptic contacts.

Sun et al. (2014) reported that very strong synaptic stimulation of the EC inputs triggered distal dendritic spikes in both CA1 and CA2 PNs. However, these spikes produced a much greater somatic depolarization in CA2 compared with CA1 PNs. A computational analysis showed that the differences in spike amplitude could be largely explained by differences in dendritic branching. Whereas the multiple secondary CA2 dendrites fired independent dendritic spikes that summated at the primary dendritic branch point, resulting in a large net spike at the CA2 soma, CA1 PNs, with only one or two apical dendrites, are capable of little or no spike summation. However, Sun et al. (2014) did not examine factors responsible for dendritic integration of the EPSP, effects of I_h, synapse number, or propagation of voltage signals along a single dendritic branch.

Our computational, electrophysiological, and immunohisto-chemical findings extend the results of Sun et al. (2014) by demonstrating how differences in propagation along single dendritic branches combined with differences in I_h and synapse number play an important role in determining the differential response of CA2 and CA1 dendrites to their cortical inputs. In CA1, I_h is largely generated by the HCN1 subunit (Santoro et al., 1997; Nolan et al., 2004). Previous work has shown that I_h (and HCN1) is strongly expressed in CA1 apical dendrites in a striking gradient of increasing expression with increasing distance from the soma

(Santoro et al., 1997; Magee, 1998, 1999) where it acts as a depolarizing shunt conductance to limit the EPSP amplitude. Because of its strong distal dendritic expression, I_h is particularly effective in suppressing the distal cortical EPSP. In contrast, we find that I_h and HCN1/HCN2 channel subunits are weakly expressed in CA2 PNs, where there is little distal dendritic enrichment. As a result, pharmacological blockade of I_h causes a substantial (~50%) enhancement in the distally evoked EPSP recorded in the soma of CA1 PNs but has little effect on EPSP amplitude in CA2 PNs.

Given the difficulty in measuring voltage directly from thin distal dendrites, we evaluated the consequences of the differences in dendritic morphology and levels of I_h by building multicompartmental models of both CA1 and CA2 PNs, using identical values of passive membrane resistance and specific intracellular resistance, and our measured neuronal morphology to explore the mechanisms and consequences of the different electrical properties. The computational model, which was fully constrained by our experimental results, faithfully reproduced the subthreshold electrophysiological properties of CA1 and CA2 PNs, implying that the differences in these properties are largely determined by differences in dendritic architecture and levels of I_h.

According to our simulations, morphological differences and differences in I_h are sufficient to account for the 2.0-fold larger somatic uEPSP elicited by glutamate uncaging at a single CA2 spine compared with the response evoked from a CA1 spine. The extent by which the dendrites attenuate a distally generated voltage signal when recorded at the soma was actually 3.0-fold greater in CA1 compared with CA2 PNs. However, because the local distal dendritic voltage response to a given synaptic conductance change was 50% larger in CA1 compared with CA2 dendrites (reflecting the higher CA1 distal input resistance), the net response at the CA2 soma was only 2.0-fold greater than in CA1. Our results do not rule out the possibility that differences in dendritic expression of other voltage-gated channels that operate under a subthreshold voltage regimen may also contribute to the differential processing of synaptic inputs in CA2 compared with CA1 PNs.

Our morphological measurements also revealed that CA2 distal dendrites possess ~3.0-fold more spines than do CA1 dendrites, suggesting a corresponding difference in the number of excitatory inputs. Importantly, the spine results do not necessarily imply a 3.0-fold larger synaptic response as the relation between the number of active inputs and the resulting EPSP will be sublinear whenever the local EPSP approaches its reversal potential (Magee, 2000; Gulledge et al., 2005; Spruston, 2008). Indeed, a key finding of our simulations is that the properties of CA2 distal dendritic compartments enable them to respond to a larger number of synaptic inputs over a linear range before reaching saturation compared with CA1 dendrites. This is because the large-diameter CA2 distal dendrites have a lower input impedance compared with the thin-diameter CA1 dendrites and, thus, generate a smaller local depolarization in response to a given number of activated inputs.

One further interesting aspect of our findings is that the greatest difference in attenuation of the distal EPSPs by CA1 compared with CA2 dendrites occurs in the proximal half of the dendrites, located in SR. Over this region, CA2 dendrites produce little additional attenuation of the EPSP, whereas the CA1 dendrites produce a 3.0-fold additional attenuation. These differences again are partly due to differences in I_h and partly due to differences in dendritic morphology (Fig. 8). At first glance, these results may appear to contradict the findings from our uncaging experiments on proximal spines located on secondary dendritic branches in

SR, which showed that the amplitude of the uEPSP was similar at the soma of CA1 and CA2 PNs (Fig. 2). However, additional simulations (data not shown) demonstrate that the local EPSP at its point of generation in the CA1 secondary oblique dendrite was much larger than that in the CA2 dendrite because of the thinner diameter and higher input resistance of the CA1 secondary oblique dendrites. The actual attenuation factor to the soma from the point where the CA1 secondary dendrite reached the primary dendrite was identical to that calculated for the distally evoked CA1 EPSP.

The direct cortical inputs are likely to play different roles in the ongoing activity of CA1 compared with CA2 PNs based on their differential depolarizing drive. In CA1, the EC inputs serve as modulators of excitation by the more powerful Schaffer collateral inputs from CA3 PNs (Remondes and Schuman, 2002; Jarsky et al., 2005). Thus, paired activation of EC and SC inputs can trigger burst firing of CA1 PNs (Takahashi and Magee, 2009), which may trigger synaptic plasticity that helps encode novel place fields (Bittner et al., 2015) and aid in memory storage and recall (Kaifosh and Losonczy, 2016). EC inputs to CA1 may also serve to enhance memory specificity (Basu et al., 2016) by inducing a powerful form of heterosynaptic plasticity of SC excitation termed input-timing-dependent plasticity (Dudman et al., 2007; Basu et al., 2013, 2016). In contrast, the EC inputs in CA2 SLM are sufficient to act as the primary drivers of CA2 output, perhaps mediating the effects of these neurons in social memory storage (Hitti and Siegelbaum, 2014; Stevenson and Caldwell, 2014; Smith et al., 2016). Such results demonstrate how the combination of synaptic and extrasynaptic dendritic properties act in concert to influence the efficacy of a given synaptic input in driving neuronal output in a compartment and input-specific manner, thereby actuating circuit-specific computations performed by distinct classes of neurons.

References

Alexander GM, Farris S, Pirone JR, Zheng C, Colgin LL, Dudek SM (2016) Social and novel contexts modify hippocampal CA2 representations of space. Nat Commun 7:10300. CrossRef Medline

Basu J, Srinivas KV, Cheung SK, Taniguchi H, Huang ZJ, Siegelbaum SA (2013) A cortico-hippocampal learning rule shapes inhibitory microcircuit activity to enhance hippocampal information flow. Neuron 79:1208– 1221. CrossRef Medline

Basu J, Zaremba JD, Cheung SK, Hitti FL, Zemelman BV, Losonczy A, Siegelbaum SA (2016) Gating of hippocampal activity, plasticity, and memory by entorhinal cortex long-range inhibition. Science 351:aaa5694. CrossRef Medline

Bittner KC, Grienberger C, Vaidya SP, Milstein AD, Macklin JJ, Suh J, Tonegawa S, Magee JC (2015) Conjunctive input processing drives feature selectivity in hippocampal CA1 neurons. Nat Neurosci 18:1133–1142. CrossRef Medline

Bloodgood BL, Sabatini BL (2007) Nonlinear regulation of unitary synaptic signals by CaV(2.3) voltage-sensitive calcium channels located in dendritic spines. Neuron 53:249–260. CrossRef Medline

Chen S, Wang J, Siegelbaum SA (2001) Properties of hyperpolarization-activated pacemaker current defined by coassembly of HCN1 and HCN2 subunits and basal modulation by cyclic nucleotide. J Gen Physiol 117: 491–504. CrossRef Medline

Chevaleyre V, Siegelbaum SA (2010) Strong CA2 pyramidal neuron synapses define a powerful disynaptic cortico-hippocampal loop. Neuron 66:560–572. CrossRef Medline

Dudman JT, Tsay D, Siegelbaum SA (2007) A role for synaptic inputs at distal dendrites: instructive signals for hippocampal long-term plasticity. Neuron 56:866–879. CrossRef Medline

Feldman ML, Peters A (1979) A technique for estimating total spine numbers on Golgi-impregnated dendrites. J Comp Neurol 188:527– 542. CrossRef Medline

Fino E, Yuste R (2011) Dense inhibitory connectivity in neocortex. Neuron 69:1188–1203. CrossRef Medline

Ganeshina O, Berry RW, Petralia RS, Nicholson DA, Geinisman Y (2004) Differences in the expression of AMPA and NMDA receptors between axospinous perforated and nonperforated synapses are related to the configuration and size of postsynaptic densities. J Comp Neurol 468:86–95. CrossRef Medline

Gasparini S, Migliore M, Magee JC (2004) On the initiation and propagation of dendritic spikes in CA1 pyramidal neurons. J Neurosci 24:11046– 11056. CrossRef Medline

Geinisman Y (1993) Perforated axospinous synapses with multiple, completely partitioned transmission zones: probable structural intermediates in synaptic plasticity. Hippocampus 3:417– 433. CrossRef Medline

George MS, Abbott LF, Siegelbaum SA (2009) HCN hyperpolarization-activated cation channels inhibit EPSPs by interactions with M-type K(+) channels. Nat Neurosci 12:577–584. CrossRef Medline

Golding NL, Mickus TJ, Katz Y, Kath WL, Spruston N (2005) Factors mediating powerful voltage attenuation along CA1 pyramidal neuron dendrites. J Physiol 568:69–82. CrossRef Medline

Gulledge AT, Kampa BM, Stuart GJ (2005) Synaptic integration in dendritic trees. J Neurobiol 64:75–90. CrossRef Medline

Harnett MT, Makara JK, Spruston N, Kath WL, Magee JC (2012) Synaptic amplification by dendritic spines enhances input cooperativity. Nature 491:599–602. CrossRef Medline

Harris KM, Stevens JK (1989) Dendritic spines of CA 1 pyramidal cells in the rat hippocampus: serial electron microscopy with reference to their biophysical characteristics. J Neurosci 9:2982–2997. Medline

Hines ML, Carnevale NT (1997) The NEURON simulation environment. Neural Comput 9:1179–1209. CrossRef Medline

Hitti FL, Siegelbaum SA (2014) The hippocampal CA2 region is essential for social memory. Nature 508:88–92. CrossRef Medline

Huang Z, Lujan R, Martinez-Hernandez J, Lewis AS, Chetkovich DM, Shah MM (2012) TRIP8b-independent trafficking and plasticity of adult cortical presynaptic HCN1 channels. J Neurosci 32:14835–14848. CrossRef Medline

Jarsky T, Roxin A, Kath WL, Spruston N (2005) Conditional dendritic spike propagation following distal synaptic activation of hippocampal CA1 pyramidal neurons. Nat Neurosci 8:1667–1676. CrossRef Medline

Kaifosh P, Losonczy A (2016) Mnemonic functions for nonlinear dendritic integration in hippocampal pyramidal circuits. Neuron 90:622– 634. CrossRef Medline

Katz Y, Menon V, Nicholson DA, Geinisman Y, Kath WL, Spruston N (2009) Synapse distribution suggests a two-stage model of dendritic integration in CA1 pyramidal neurons. Neuron 63:171–177. CrossRef Medline

Kay K, Sosa M, Chung JE, Karlsson MP, Larkin MC, Frank LM (2016) A hippocampal network for spatial coding during immobility and sleep. Nature 531:185–190. CrossRef Medline

Kharazia VN, Weinberg RJ (1999) Immunogold localization of AMPA and NMDA receptors in somatic sensory cortex of albino rat. J Comp Neurol 412:292–302. CrossRef Medline

Lewis AS, Vaidya SP, Blaiss CA, Liu Z, Stoub TR, Brager DH, Chen X, Bender RA, Estep CM, Popov AB, Kang CE, Van Veldhoven PP, Bayliss DA, Nicholson DA, Powell CM, Johnston D, Chetkovich DM (2011) Deletion of the hyperpolarization-activated cyclic nucleotide-gated channel auxiliary subunit TRIP8b impairs hippocampal Ih localization and function and promotes antidepressant behavior in mice. J Neurosci 31:7424– 7440. CrossRef Medline

London M, Häusser M (2005) Dendritic computation. Annu Rev Neurosci 28:503–532. CrossRef Medline

Lörincz A, Notomi T, Tamás G, Shigemoto R, Nusser Z (2002) Polarized and compartment-dependent distribution of HCN1 in pyramidal cell dendrites. Nat Neurosci 5:1185–1193. CrossRef Medline

Ludwig A, Budde T, Stieber J, Moosmang S, Wahl C, Holthoff K, Langebartels A, Wotjak C, Munsch T, Zong X, Feil S, Feil R, Lancel M, Chien KR, Konnerth A, Pape HC, Biel M, Hofmann F (2003) Absence epilepsy and sinus dysrhythmia in mice lacking the pacemaker channel HCN2. EMBO J 22:216–224. CrossRef Medline

Magee JC (1998) Dendritic hyperpolarization-activated currents modify the integrative properties of hippocampal CA1 pyramidal neurons. J Neurosci 18:7613–7624. Medline

Magee JC (1999) Dendritic *Ih* normalizes temporal summation in hippocampal CA1 neurons. Nat Neurosci 2:848. CrossRef Medline

Magee JC (2000) Dendritic integration of excitatory synaptic input. Nat Rev Neurosci 1:181–190. CrossRef Medline

Mainen ZF, Sejnowski TJ (1996) Influence of dendritic structure on firing pattern in model neocortical neurons. Nature 382:363–366. CrossRef Medline

Mankin EA, Diehl GW, Sparks FT, Leutgeb S, Leutgeb JK (2015) Hippocampal CA2 activity patterns change over time to a larger extent than between spatial contexts. Neuron 85:190–201. CrossRef Medline

Matsuzaki M, Ellis-Davies GC, Nemoto T, Miyashita Y, Iino M, Kasai H (2001) Dendritic spine geometry is critical for AMPA receptor expression in hippocampal CA1 pyramidal neurons. Nat Neurosci 4:1086–1092. CrossRef Medline

Megías M, Emri Z, Freund TF, Gulyás AI (2001) Total number and distribution of inhibitory and excitatory synapses on hippocampal CA1 pyramidal cells. Neuroscience 102:527–540. CrossRef Medline

Neuman KM, Molina-Campos E, Musial TF, Price AL, Oh KJ, Wolke ML, Buss EW, Scheff SW, Mufson EJ, Nicholson DA (2015) Evidence for Alzheimer's disease-linked synapse loss and compensation in mouse and human hippocampal CA1 pyramidal neurons. Brain Struct Funct 220:3143–3165. CrossRef Medline

Nicholson DA, Geinisman Y (2009) Axospinous synaptic subtype-specific differences in structure, size, ionotropic receptor expression, and connectivity in apical dendritic regions of rat hippocampal CA1 pyramidal neurons. J Comp Neurol 512:399–418. CrossRef Medline

Nolan MF, Malleret G, Dudman JT, Buhl DL, Santoro B, Gibbs E, Vronskaya S, Buzsáki G, Siegelbaum SA, Kandel ER, Morozov A (2004) A behavioral role for dendritic integration: HCN1 channels constrain spatial memory and plasticity at inputs to distal dendrites of CA1 pyramidal neurons. Cell 119:719–732. CrossRef Medline

Notomi T, Shigemoto R (2004) Immunohistochemical localization of Ih channel subunits, HCN1–4, in the rat brain. J Comp Neurol 471:241–276. CrossRef Medline

Pagani JH, Zhao M, Cui Z, Avram SK, Caruana DA, Dudek SM, Young WS (2015) Role of the vasopressin 1b receptor in rodent aggressive behavior and synaptic plasticity in hippocampal area CA2. Mol Psychiatry 20:490–499. CrossRef Medline

Piskorowski R, Santoro B, Siegelbaum SA (2011) TRIP8b splice forms act in concert to regulate the localization and expression of HCN1 channels in CA1 pyramidal neurons. Neuron 70:495–509. CrossRef Medline

Poolos NP, Migliore M, Johnston D (2002) Pharmacological upregulation of h-channels reduces the excitability of pyramidal neuron dendrites. Nat Neurosci 5:767–774. CrossRef Medline

Remondes M, Schuman EM (2002) Direct cortical input modulates plasticity and spiking in CA1 pyramidal neurons. Nature 416:736–740. CrossRef Medline

Routh BN, Johnston D, Harris K, Chitwood RA (2009) Anatomical and electrophysiological comparison of CA1 pyramidal neurons of the rat and mouse. J Neurophysiol 102:2288–2302. CrossRef Medline

Santoro B, Grant SG, Bartsch D, Kandel ER (1997) Interactive cloning with the SH3 domain of N-src identifies a new brain specific ion channel protein, with homology to eag and cyclic nucleotide-gated channels. Proc Natl Acad Sci U S A 94:14815–14820. CrossRef Medline

Santoro B, Chen S, Luthi A, Pavlidis P, Shumyatsky GP, Tibbs GR, Siegelbaum SA (2000) Molecular and functional heterogeneity of hyperpolarization-activated pacemaker channels in the mouse CNS. J Neurosci 20:5264–5275. Medline

Santoro B, Wainger BJ, Siegelbaum SA (2004) Regulation of HCN channel surface expression by a novel C-terminal protein–protein interaction. J Neurosci 24:10750–10762. CrossRef Medline

Santoro B, Piskorowski RA, Pian P, Hu L, Liu H, Siegelbaum SA (2009) TRIP8b splice variants form a family of auxiliary subunits that regulate gating and trafficking of HCN channels in the brain. Neuron 62:802–813. CrossRef Medline

Smith AS, Williams Avram SK, Cymerblit-Sabba A, Song J, Young WS (2016) Targeted activation of the hippocampal CA2 area strongly enhances social memory. Mol Psychiatry 21:1137–1144. CrossRef Medline

Spruston N (2008) Pyramidal neurons: dendritic structure and synaptic integration. Nat Rev Neurosci 9:206–221. CrossRef Medline

Spruston N, Jonas P, Sakmann B (1995) Dendritic glutamate receptor channels in rat hippocampal CA3 and CA1 pyramidal neurons. J Physiol 482:325–352. CrossRef Medline

Stevenson EL, Caldwell HK (2014) Lesions to the CA2 region of the hippocampus impair social memory in mice. Eur J Neurosci 40:3294–3301. CrossRef Medline

Stiefel KM, Sejnowski TJ (2007) Mapping function onto neuronal morphology. J Neurophysiol 98:513–526. CrossRef Medline

Stuart G, Spruston N (1998) Determinants of voltage attenuation in neocortical pyramidal neuron dendrites. J Neurosci 18:3501–3510. Medline

Stuart GJ, Spruston N (2015) Dendritic integration: 60 years of progress. Nat Neurosci 18:1713–1721. CrossRef Medline

Sun Q, Srinivas KV, Sotayo A, Siegelbaum SA (2014) Dendritic Na spikes enable cortical input to drive action potential output from hippocampal CA2 pyramidal neurons. eLife 3.

Takahashi H, Magee JC (2009) Pathway interactions and synaptic plasticity in the dendritic tuft regions of CA1 pyramidal neurons. Neuron 62:102–111. CrossRef Medline

Wilkars W, Liu Z, Lewis AS, Stoub TR, Ramos EM, Brandt N, Nicholson DA, Chetkovich DM, Bender RA (2012) Regulation of axonal HCN1 trafficking in perforant path involves expression of specific TRIP8b isoforms. PLoS One 7:e32181. CrossRef Medline

Witter MP, Canto CB, Couey JJ, Koganezawa N, O'Reilly KC (2014) Architecture of spatial circuits in the hippocampal region. Philos Trans R Soc Lond B Biol Sci 369:20120515. CrossRef Medline

Yeckel MF, Berger TW (1995) Monosynaptic excitation of hippocampal CA1 pyramidal cells by afferents from the entorhinal cortex. Hippocampus 5:108–114. CrossRef Medline

Zolles G, Wenzel D, Bildl W, Schulte U, Hofmann A, Müller CS, Thumfart JO, Vlachos A, Deller T, Pfeifer A, Fleischmann BK, Roeper J, Fakler B, Klöcker N (2009) Association with the auxiliary subunit PEX5R/Trip8b controls responsiveness of HCN channels to cAMP and adrenergic stimulation. Neuron 62:814–825. CrossRef Medline